

1 **Trace Organic Gas Analyzer Time-of-Flight mass spectrometer**  
2 **(TOGA-TOF) system for airborne observations of formaldehyde**

3  
4 Daun Jeong<sup>1,a,b</sup>, Rebecca S. Hornbrook<sup>2,\*</sup>, Alan J. Hills<sup>2</sup>, Glenn Diskin<sup>3</sup>, Hannah S. Halliday<sup>3</sup>,  
5 Joshua P. DiGangi<sup>3</sup>, Alan Fried<sup>4</sup>, Dirk Richter<sup>4</sup>, James Walega<sup>4</sup>, Petter Weibring<sup>4</sup>, Thomas F.  
6 Hanisco<sup>5</sup>, Glenn M. Wolfe<sup>5</sup>, Jason St. Clair<sup>5</sup>, Jeff Peischl<sup>6,c</sup>, Armin Wisthaler<sup>7,8</sup>, Tomas  
7 Mikoviny<sup>7</sup>, John B. Nowak<sup>3</sup>, Felix Piel<sup>7</sup>, Laura Tomsche<sup>3</sup>, Christopher D. Holmes<sup>9</sup>, Amber  
8 Soja<sup>3</sup>, Emily Gargulinski<sup>10</sup>, James H. Crawford<sup>3</sup>, Jack Dibb<sup>11</sup>, Carsten Warneke<sup>12</sup>, Joshua  
9 Schwarz<sup>12</sup>, and Eric C. Apel<sup>2,\*</sup>

10 <sup>1</sup>Advanced Study Program, NSF National Center for Atmospheric Research, Boulder, CO, USA

11 <sup>2</sup>Atmospheric Chemistry Observations & Modeling Laboratory, NSF National Center for Atmospheric  
12 Research, Boulder, CO, USA

13 <sup>3</sup>NASA Langley Research Center, Hampton, VA, USA

14 <sup>4</sup>Institute of Arctic and Alpine Research, University of Colorado, Boulder, CO, USA

15 <sup>5</sup>NASA Goddard Space Flight Center, Greenbelt, MD, USA

16 <sup>6</sup>Cooperative Institute for Research in Environmental Sciences, University of Colorado, Boulder, CO,  
17 USA

18 <sup>7</sup>Department of Chemistry, University of Oslo, Oslo, Norway

19 <sup>8</sup>Institute for Ion Physics and Applied Physics, University of Innsbruck, Innsbruck, Austria

20 <sup>9</sup>Department of Earth, Ocean, and Atmospheric Science, Florida State University, Tallahassee, FL, USA

21 <sup>10</sup>National Institute of Aerospace, Hampton, VA, USA

22 <sup>11</sup>Earth Systems Research Center, University of New Hampshire, Durham, NH, USA

23 <sup>12</sup>Chemical Science Laboratory, National Oceanic and Atmospheric Administration (NOAA), Boulder,  
24 CO, USA

25 <sup>a</sup>now at: Cooperative Institute for Research in Environmental Sciences, University of Colorado, Boulder,  
26 CO, USA

27 <sup>b</sup>now at: Chemical Science Laboratory, National Oceanic and Atmospheric Administration (NOAA),  
28 Boulder, CO, USA

29 <sup>c</sup>now at: Global Monitoring Laboratory, National Oceanic and Atmospheric Administration (NOAA),  
30 Boulder, CO, USA

31  
32 \*Corresponding Authors: Eric C. Apel and Rebecca S. Hornbrook  
33 Atmospheric Chemistry Observations & Modeling Laboratory,  
34 NSF National Center for Atmospheric Research, Boulder, CO 80307 USA

35 [apel@ucar.edu](mailto:apel@ucar.edu)

36 [rsh@ucar.edu](mailto:rsh@ucar.edu)

37 Submission to: *Atmospheric Measurement Techniques*

38 Keywords: FIREX-AQ, formaldehyde, TOGA-TOF, biomass burning

39  
40

41 **Abstract**

42 Formaldehyde (HCHO) is a ubiquitous atmospheric constituent, originating from primary  
43 emissions (natural and anthropogenic) and secondary production via the oxidation of volatile  
44 organic compounds (VOCs). In addition to being a regulated pollutant, HCHO is a key species  
45 used as a tracer of recent photochemical activity due to its short atmospheric lifetime and its role  
46 as a source of HO<sub>x</sub> radicals. Given its diverse sources and high spatial variability, HCHO is  
47 challenging to represent accurately in chemical transport models, often resulting in significant  
48 discrepancies with observations. Airborne *in-situ* measurements of HCHO, especially when  
49 combined with VOC precursor data, offer valuable insights into its atmospheric distributions for  
50 evaluating models. Here, we present HCHO observations from the NSF NCAR Trace Organic  
51 Gas Analyzer with Time-of-Flight mass spectrometer (TOGA-TOF), deployed during the 2019  
52 Fire Influence on Regional to Global Environments and Air Quality (FIREX-AQ) campaign.  
53 While most HCHO instruments target at most a few selected species for measurement, the TOGA-  
54 TOF employs a rapid gas chromatography-mass spectrometry (GC/MS) technique and provides  
55 discrete VOC measurements—including >100 C<sub>1</sub>-C<sub>10</sub> species—at a time resolution of less than  
56 2 minutes. We compare TOGA-TOF HCHO data to measurements from three 1-Hz instruments  
57 aboard the NASA DC-8: the Compact Atmospheric Multi-species Spectrometer (CAMS), the In  
58 Situ Airborne Formaldehyde (ISAF) instrument, and a proton-transfer-reaction time-of-flight  
59 mass spectrometer (PTR-ToF-MS). The wide dynamic range of observed HCHO concentrations  
60 (from < 100 ppt to ~100 ppb) during FIREX-AQ enabled a robust intercomparison. TOGA-TOF  
61 HCHO agreed well with CAMS (slope = 1.1), with similar agreement with the PTR-ToF-MS,  
62 while larger discrepancies were observed with ISAF (slope = 1.5), likely due to differences in  
63 calibrations. Normalized excess mixing ratios (NEMRs) of HCHO relative to CO in wildfire  
64 plumes exhibited consistent trends with plume age across instruments. These findings highlight  
65 the TOGA-TOF's capability for highly sensitive and accurate airborne HCHO measurements.

Formatted: Font: Italic

66 **1. Introduction**

67 Formaldehyde (HCHO) is one of the most ubiquitous non-methane volatile organic  
68 compounds (VOCs) in the atmosphere. In addition to being an EPA regulated pollutant (National  
69 Research Council (US) Committee on Toxicology, 1980), HCHO is a key reactive compound in

70 understanding recent photochemistry in the atmosphere. HCHO is an oxidation product of a wide  
71 range of VOCs, has a relatively short lifetime, and is an important source of HO<sub>x</sub> (OH + HO<sub>2</sub>),  
72 therefore affecting NO<sub>x</sub>-VOC-O<sub>3</sub> chemistry (Seinfeld and Pandis, 2006). Globally, the dominant  
73 source of HCHO is secondary production from VOC oxidation (Luecken et al., 2012; Stavrou  
74 et al., 2009). Tropospheric background levels of HCHO are maintained through methane (CH<sub>4</sub>)  
75 (Stavrou et al., 2009) and isoprene (C<sub>5</sub>H<sub>8</sub>) (Curci et al., 2010; Luecken et al., 2018; Palmer et  
76 al., 2003; Wolfe et al., 2016) oxidation. Direct emissions of HCHO can also be important locally;  
77 sources include vehicle emissions (Possanzini et al., 2002; Sagebiel et al., 1996; Viskari et al.,  
78 2000), biomass burning (Lee et al., 1997; Zhang et al., 2013), and fossil fuel industries (Fried et  
79 al., 2020; Green et al., 2021; Pfister et al., 2019). In the atmosphere, HCHO is mainly lost through  
80 photolysis, reaction with OH, and deposition, resulting in daytime atmospheric lifetimes of 1 to 9  
81 hours (1–3 hours midday).

82 As an important proxy for understanding recent photochemistry, HCHO observations have  
83 been used to indicate ozone sensitivity regimes (VOC- or NO<sub>x</sub>-limited) (Duncan et al., 2010;  
84 Martin et al., 2004; Nussbaumer et al., 2021; Schroeder et al., 2017; Souri et al., 2020, 2023) as  
85 well as top-down estimations of isoprene (Cao et al., 2018; Kaiser et al., 2018; Palmer et al., 2003;  
86 Wolfe et al., 2016; Zhu et al., 2016) and anthropogenic VOC (Cao et al., 2018; Kwon et al., 2021)  
87 emissions. While satellite retrievals of HCHO column densities have been widely used in these  
88 methods, challenges remain in capturing the spatial (vertical and horizontal) representation of  
89 HCHO over the wide mixing ratio (MR) range observed in the troposphere; HCHO MRs can vary  
90 less from than 20 parts per trillion (ppt) in remote regions, 1–20 parts per billion (ppb) in urban  
91 environments, and > 100 ppb in fire plumes as observed from aircraft. These challenges in HCHO  
92 satellite observations have been driven by uncertainties in retrieval methods (Anderson et al., 2017;

93 Liao et al., 2025; Souri et al., 2023; Stavrou et al., 2009; Zhu et al., 2016), instrument sensitivity  
94 (Souri et al., 2023), and coarse pixel sizes (Kwon et al., 2021; Souri et al., 2023). Uncertainties in  
95 satellite observations increase in environments with low HCHO, such as regions with weak  
96 biogenic or anthropogenic sources (Souri et al., 2023). Three-dimensional chemical transport  
97 models may also fail to reproduce observed HCHO levels due to inaccurate emission inventories  
98 of direct HCHO emissions or its VOC precursors (Green et al., 2021; Jaeglé et al., 2018; Luecken  
99 et al., 2012, 2018; Warneke et al., 2007), uncertainties in chemical mechanisms (Luecken et al.,  
100 2012), and coarse grid size. High quality *in-situ* HCHO observations during airborne field  
101 campaigns can provide useful information to validate satellite observations and evaluate chemical  
102 transport models (Anderson et al., 2017; Chan Miller et al., 2017; Schroeder et al., 2017; Souri et  
103 al., 2023; Zhu et al., 2016). For example, recent studies on HCHO intercomparisons between  
104 satellite and *in-situ* airborne observations showed that satellite HCHO retrievals can have a  
105 systematic low bias of -20 to -51% (Anderson et al., 2017; Zhu et al., 2016), which can lead to  
106 underestimation of VOC emissions. These systematic biases in satellite observations can be  
107 corrected using high-quality airborne *in-situ* observations of HCHO (Chan Miller et al., 2017;  
108 Zhu et al., 2016, 2017).

109 Biomass burning produces large amounts of HCHO both from primary emissions and  
110 secondary production. During a biomass burning event, a highly complex mixture of VOCs (Akagi  
111 et al., 2011; Gilman et al., 2015; Gkatzelis et al., 2024; Koss et al., 2018; Travis et al., 2023;  
112 Yokelson et al., 2013a) is produced from the fire source, which subsequently undergoes complex  
113 chemical (i.e., reaction with oxidants and photolysis) and physical (i.e., dilution and cooling)  
114 transformations downwind of the source (Decker et al., 2021; Hornbrook et al., 2011; Robinson et  
115 al., 2021; Wang et al., 2021). For the recent joint NOAA/NASA Fire Influence on Regional to

116 Global Environments and Air Quality (FIREX-AQ) mission, Wang et al. (2021) used a high-  
117 resolution large eddy simulation (LES) to show the chemical complexity of a fresh wildfire plume.  
118 The levels and types of predominant oxidants, which are dependent on the historic exposure to  
119 light, varies with the evolution of a plume, affecting the chemistry and fate of trace gases and  
120 aerosols (Decker et al., 2021; Robinson et al., 2021; Wang et al., 2021). Liao et al. (2021) showed  
121 that primary emissions of HCHO dominate near the fire source but secondary production from  
122 VOC oxidation becomes important (up to ~60% after a few hours of physical age) as the fire ages.  
123 As reported by Travis et al. (2023), the MRs of different types of VOCs emitted in crop and  
124 prescribed fire plumes during FIREX-AQ depends on fuel types and fire states. The physical and  
125 chemical complexities in fire plumes ensure that HCHO MRs are highly dynamic presenting  
126 challenges for satellite retrievals (Stavrakou et al., 2009) and models to accurately represent local  
127 and regional distributions of HCHO.

128 In this study, we present the NSF NCAR Trace Organic Gas Analyzer Time-of-Flight mass  
129 spectrometer (TOGA-TOF) as a fast online GC/MS (gas chromatography-mass spectrometry)  
130 technique for airborne observations of HCHO. Studies on improved techniques to detect HCHO  
131 have been ongoing, attesting to its analytical challenges (Gilpin et al., 1997; Hopkins et al., 2003;  
132 Hunter et al., 1999; Rice and Quay, 2006). While most currently available instrumental techniques  
133 are specialized in detecting HCHO, the TOGA-TOF routinely measures over a hundred VOCs  
134 using a non-reactive concentration technique, with the capability to analyze untargeted  
135 compounds. Thus, TOGA-TOF is a unique airborne standalone instrument for the identification  
136 and quantification of a wide range of C<sub>1</sub>-C<sub>10</sub> VOCs, including formaldehyde, in complex ambient  
137 air samples. The NOAA/NASA FIREX-AQ campaign (July to September 2019) was the first  
138 campaign in which the TOGA-TOF was deployed for airborne measurements. During FIREX-AQ,

139 we had the opportunity to measure alongside two state-of-the-art HCHO measurement systems  
140 aboard the NASA DC-8 during the entire FIREX-AQ campaign: the NASA In Situ Airborne  
141 Formaldehyde (ISAF) instrument (Cazorla et al., 2015) and the University of Colorado Compact  
142 Atmospheric Multi-species Spectrometer (CAMS) (Richter et al., 2015). The University of Oslo  
143 Proton-Transfer Reaction Time-of-Flight Mass Spectrometer (UiO PTR-ToF-MS) (Müller et al.,  
144 2014) measured HCHO for select time periods as well. For this study, we present the TOGA-TOF  
145 HCHO data and focus on intercomparisons with CAMS and ISAF but also include comparisons  
146 with the UiO PTR-ToF-MS. The FIREX-AQ dataset is an excellent testbed to compare a wide  
147 range of HCHO mixing ratios (below 100 ppt to ~100 ppb) in a spatially variable ambient  
148 atmosphere. The technique used in the TOGA-TOF could, in principle, be implemented in many  
149 existing online GC/MS systems for semi-routine measurements of HCHO.

## 150 **2. Methods**

151 The sample preconcentration system in the TOGA-TOF is similar to the earlier generation  
152 TOGA instrument with a quadrupole mass analyzer, which has been described in the literature  
153 (Apel et al., 2015). The TOGA-TOF has been extensively characterized in the lab prior to and post  
154 FIREX-AQ. Here, we describe the basic operation techniques of the TOGA-TOF system (**Sect.**  
155 **2.1**), summarize the HCHO measurements during FIREX-AQ (**Sect. 2.2**), calculate the weighted  
156 averages for direct comparisons between instruments with different sampling time resolution  
157 (**Sect. 2.3**), and derive normalized excess mixing ratios (NEMR) of HCHO from selected plume  
158 transects (**Sect. 2.4**).

159 **2.1 Description of the NSF NCAR Trace Organic Gas Analyzer with Time-of-Flight Mass**  
160 **Spectrometer (TOGA-TOF)**

161 The TOGA-TOF hardware consists of a cryogenic preconcentration system, gas  
162 chromatograph (GC), time-of-flight (TOF) mass analyzer (TOFWERK, Switzerland), electronics  
163 box, clean air generator and on-board calibration system (CAG), and pump box. All major  
164 components except the TOF mass analyzer are custom built. Typical preconcentration and GC  
165 analysis sequences for the system are shown in **Fig. 1** and the flows for each sequence are shown  
166 in **Fig. 2**. The GC analysis, including temperature ramp and cool and sample preconcentration  
167 steps, occur simultaneously, with the full cycle duration of both processes time synced (**Fig. 1**) to  
168 less than 2 min. During FIREX-AQ, the runtime for one full cycle was 105 seconds including 33  
169 seconds of sample collection (i.e., “sampling”). The preconcentration system consists of three  
170 cryogenically-cooled traps as described by Apel et al. (2015): (1) a water trap for removal of water  
171 in ambient sampled air, (2) a sample trap for enrichment of targeted VOCs in ambient air, and (3)  
172 a cryofocusing trap to refocus the analytes prior to injection into the GC. Corresponding to each  
173 temperature setpoint described in **Fig. 1**, the cooling of each trap is achieved by metering the flow  
174 of gas-phase N<sub>2</sub> generated from the headspace of the TOGA-TOF Dewar through coils at the  
175 bottom of the dewar that were immersed in liquid N<sub>2</sub> (Apel et al., 2015). To heat the traps, the cold  
176 N<sub>2</sub> gas flow was first shut off and followed by PID controlled flow of electricity, via a  
177 WATLOW™ (Anafaze MLS300) temperature controller, through resistive wires wrapped around  
178 the traps. The sample trap is packed with glass wool to allow greater surface area for the  
179 enrichment of VOCs when cooling the trap to -140°C (**Fig. 1**), while allowing bulk gases such as  
180 oxygen and nitrogen to pass through unretained. Both the water trap (inner diameter (I.D.) = 0.04  
181 in.) and cryofocusing trap (I.D. = 0.021 in.) are open tubes.

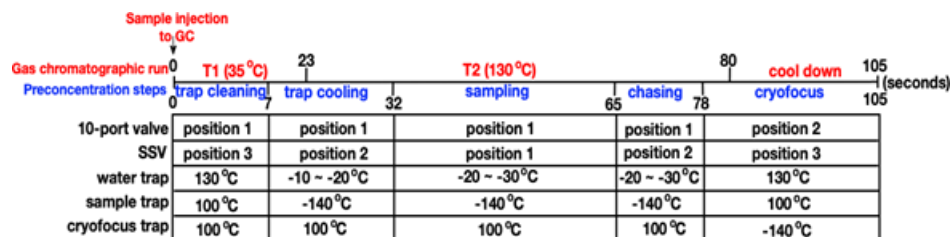


**Figure 1.** TOGA-TOF operational sequences for the gas chromatograph temperature program (red) and the preconcentration steps (blue). The position of the valves (10-port valve and stream selector valve; SSV) and temperatures of each trap are shown for each step. The duration of each sequence corresponds to the normal sampling mode timing during FIREX-AQ.

182

183 For chromatography, a Restek MXT-624 column (I.D. = 0.18 mm, length = 8 m) is used  
 184 with helium as the carrier gas. The GC column has two temperature set points with temperatures  
 185 ranging between 35°C and 130°C (**Fig. 1**), also controlled by the Watlow, allowing gas-phase C<sub>1</sub>  
 186 to C<sub>10</sub> VOCs to sequentially elute from the column. This allows the separation of VOCs, including  
 187 many structural isomers with the same chemical formula, based on their differences in interaction  
 188 with the stationary phase of the column. For detection of VOCs, the GC is coupled to a high-  
 189 resolution electron ionization time-of-flight mass spectrometer (HR EI-TOF-MS; TOFWERK),  
 190 using 70 eV ionization resulting in classical electron ionization (EI) spectra of the compounds.  
 191 This methodology allows routine quantification of well over 100 VOCs with the ability to further  
 192 analyze additional C<sub>1</sub> to C<sub>10</sub> compounds within the detectable range. Fluctuations in sensitivity are  
 193 corrected by normalizing with ambient levels of tetrachloromethane (CCl<sub>4</sub>) [based on the](#)  
 194 [recommendations in Karbiwnyk et al. \(2003\)](#). Background corrections are made by system  
 195 generated ultra-pure helium (“He mode”) and zero-air blanks and then subtracting average blank  
 196 peak areas from ambient samples. For all surfaces that the sample contacts, Restek Sulfinert® steel  
 197 tubing is used to minimize interactions. Data processing is performed using Tofware (Aerodyne  
 198 Research, Inc., Billerica, MA) for high resolution peak fitting and TERN-in-IGOR (Claflin et al.,

199 2021; Isaacman-VanWertz et al., 2017; Lerner et al., 2017) (Aerodyne Research, Inc.) for  
 200 chromatographic peak analysis.

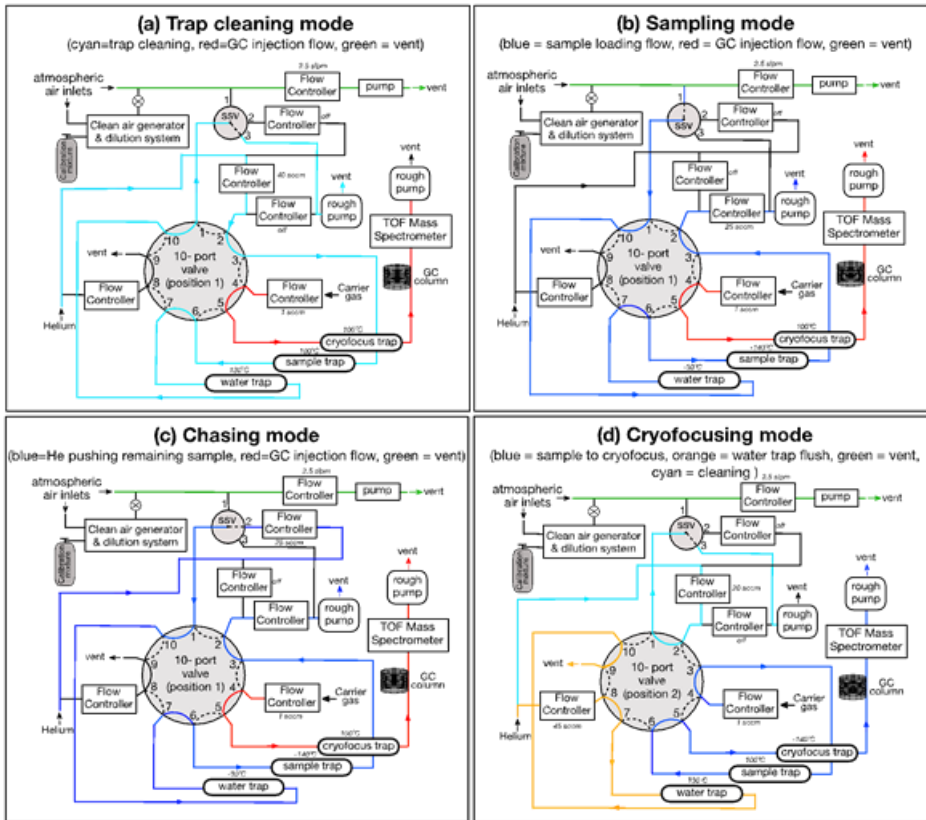


**Figure 2.** Simplified flow diagram of TOGA-TOF showing flows and temperatures of each trap during (a) trap cleaning mode, (b) sampling mode, (c) chasing mode, and (d) cryofocusing mode, corresponding to the sequence in Fig. 1.

201

202 **2.2 Description of HCHO and CO measurements during FIREX-AQ**

203 In this section, we describe the TOGA-TOF HCHO measurements during FIREX-AQ

204 (July–September 2019). FIREX-AQ (Warneke et al., 2023;

205 <https://asdc.larc.nasa.gov/project/FIREX-AQ>) focused on the emissions of trace gases and

206 particles from wildland, prescribed, and agricultural fires in the United States. The NASA DC-8  
207 flights during FIREX-AQ were based out of Boise, ID, mainly focusing on Western U.S. fires, and  
208 Salina, KS, focusing on southeastern U.S. agricultural fires (flight tracks shown in **Fig. S1**). Details  
209 on the field campaign may be found in Warneke et al. (2023).

210 As described in **Sect. 2.1**, the TOGA-TOF uses electron ionization for the detection of  
211 VOCs. The EI of HCHO results in a spectrum of its parent ion ( $m/z$  30) and major fragments ( $m/z$   
212 28 and 29) (**Fig. S2a**). **Figure S2b** shows the chromatographic signals of  $\text{CH}_2\text{O}^+$  ( $m/z$  30; exact  
213 mass 30.010016 amu) and  $\text{CHO}^+$  ( $m/z$  29; exact mass 29.002191 amu) eluting at  $\sim 20$  s. The high  
214 resolution (HR)-TOF allows detection of highly resolved ions and the Tofware peak fitting  
215 analysis shows separate parent and dominant fragments from other adjacent peaks (**Fig. S2c**).  
216 HCHO calibration was carried out using a HCHO in  $\text{N}_2$  gas-phase mixture contained in a treated  
217 aluminum cylinder (Apel-Riemer Environmental, Inc.), diluted with ultra-high purity  $\text{N}_2$ . The  
218 stated HCHO concentration of the calibration mixture cylinder from the company was 1.69 ppmv.  
219 The concentration was checked using three independent methods within a two-month period using:  
220 (1) Fourier transform infrared spectroscopy (FTIR – NSF NCAR ACOM direct absorption using  
221 the Beer-Lambert law, 1.55 ppmv), (2) Mid-IR – University of Colorado – also direct absorption  
222 employing the CAMS instrument (1.65 ppm), and (3) an EPA 2,4-dinitrophenylhydrazine (DNPH)  
223 cartridge method (1.64 ppmv). For methods (1) and (2), quantification of HCHO relies on the  
224 absolute IR cross section and thus does not require an external standard. Therefore, these can be  
225 regarded as fully independent reference methods. For the calibration of TOGA-TOF we used the  
226 averaged value of 1.61 ppmv from the three quantification methods, and the resulting calibration  
227 curve is shown in **Fig. S3**. The TOGA-TOF HCHO lower limit of detection (LLOD) during  
228 FIREX-AQ was 20 ppt, and the HCHO measurement had an uncertainty of 35% based on the

229 variability of repeat calibrations using a 1.6 ppm (parts per million) HCHO in N<sub>2</sub> standard mixture  
230 and a 90 ppb HCHO in N<sub>2</sub> standard mixture (both Apel-Reimer, Inc.), dynamically diluted to MRs  
231 ranging between 0.15 and 100 ppb using (1) the CAG (i.e., catalytically-scrubbed ambient air), (2)  
232 dry N<sub>2</sub>, and (3) humidified N<sub>2</sub>. No humidity dependence was observed.

233 HCHO mixing ratios from the TOGA-TOF were compared to 1-Hz HCHO measurements  
234 from the ISAF, CAMS, and UiO PTR-ToF-MS instruments onboard the DC-8. The ISAF  
235 instrument was operated by NASA and the details on the instrumental technique are described in  
236 Cazorla et al. (2015). Briefly, the ISAF instrument uses a laser-induced fluorescence technique to  
237 quantify HCHO using the fluorescence resulting from excitation of HCHO at 353 nm with a  
238 tunable UV laser. Backgrounds were determined from the offline position 0.005 nm away from  
239 the peak. Calibrations were made using a compressed HCHO gas cylinder (Air Liquide, 584 ppbv)  
240 quantified by FTIR (Liao et al., 2021). ISAF was operated at a native sampling rate of 10-Hz and  
241 archived at 10-Hz and 1-Hz. We used the 1-Hz data for analysis. The reported LLOD of HCHO  
242 measured by ISAF is 30 ppt for the 1-Hz data at a signal/noise = 1 and the accuracy (systematic  
243 uncertainty) of the ISAF measurements is estimated to be 10% + 10 ppt. More details on the ISAF  
244 HCHO measurement during FIREX-AQ can be found in Liao et al. (2021).

245 The CAMS was operated by the University of Colorado and a detailed description of the  
246 system can be found in the work of Richter et al. (2015). The CAMS uses a tunable IR laser source  
247 for generation of mid-IR light for the detection of HCHO based on absorption. Background spectra  
248 were collected during flights using zero air from a scrubber and were subtracted from the ambient  
249 spectra. Calibrations were carried out by using a 4.9 ppm HCHO standard in N<sub>2</sub>, quantified by  
250 direct absorption using the Beer-Lambert law. The reported uncertainty of the FIREX-AQ HCHO  
251 CAMS measurements is 6% and the campaign-averaged LLOD is 110 ppt for 1-Hz measurements

252 at a signal/noise = 1 during FIREX-AQ. However, during previous airborne missions (e.g.,  
253 KORUS-AQ; Fried et al., 2020), LLODs ranging from 28 to 80 ppt have been reported. The  
254 degraded performance during FIREX-AQ resulted from dirty multipass cell mirrors.

255 The UiO PTR-ToF-MS (Müller et al., 2014) was operated by the University of Oslo with  
256 a focus on measuring NH<sub>3</sub> during FIREX-AQ, although HCHO and a number of additional VOCs  
257 were reported for select flights (i.e., 25 July and 3 August). The PTR-ToF-MS uses hydronium  
258 ions (H<sub>3</sub>O<sup>+</sup>) generated from water vapor in a glow discharge-drift-tube to detect VOCs through  
259 nondissociative proton transfer reactions. HCHO calibrations were carried out using a gas-phase  
260 HCHO in N<sub>2</sub> cylinder (Apel-Riemer Environmental, Inc., 9.6 ppm HCHO; ± 5%). This calibration  
261 was checked post-mission by generating test atmospheres with five different HCHO mixing ratios  
262 (145–1035 ppb) in a 250-L laboratory chamber. The chamber was equipped with a White cell type  
263 multiple reflection mirror system with a 120-m optical path length for online detection with a  
264 Bruker IFS 66v/S FTIR instrument. The two methods were in excellent agreement, with the PTR-  
265 ToF-MS reporting a volume mixing ratios less than 3% higher than the FTIR. During the two flight  
266 days (25 July and 3 August) the UiO PTR-ToF-MS measured HCHO; the slope of the retrieved  
267 ambient HCHO relative to that from CAMS was 1.03.

268 Normalized excess mixing ratios (NEMRs) of HCHO to CO are calculated as described in  
269 **Sect. 2.4**. CO measurements were made onboard the DC-8 using the NOAA Los Gatos Research  
270 (LGR) CO instrument and the NASA Differential Absorption Carbon monOxide Measurement  
271 (DACOM) instruments. The LGR instrument (Bourgeois et al., 2022) uses an infrared laser off-  
272 axis integrated-cavity-output spectroscopy technique with a time response of 1-Hz. The DACOM  
273 instrument uses a differential absorption technique with an infrared tunable diode laser detecting  
274 CO at the 4.7 μm wavelength, giving a data frequency of 5-Hz and measurement uncertainty of

275 2% (Sachse et al., 1987). The two CO instruments were in excellent agreement with the coefficient  
276 of determination  $r^2 = 0.97$ , and a slope of 0.97 during the entirety of the campaign (Fig. S4), with  
277 the reported LGR CO consistently 2.2% below that of DACOM.

### 278 2.3 Averaging methods for comparison of HCHO between different instruments

279 Data averaging across various sampling time periods is often carried out for direct  
280 comparison between instrumental techniques with different sample integration times. Figure 3  
281 shows HCHO measured by TOGA-TOF and ~~ISAF-CAMS~~ with LGR CO measurements during  
282 plume transects from the Castle Fire (Fig. 3a) and the Williams Flats Fire (Fig. 3b). As described  
283 in Sect. 2.1, during FIREX-AQ, the TOGA-TOF took discrete samples for 33 seconds in a 105-  
284 second cycle period; therefore, subsections of each plume transect were sampled for analysis (Fig.  
285 3). To directly compare the discrete TOGA-TOF HCHO sampling data, CAMS, ISAF, and UiO  
286 PTR-ToF-MS 1-Hz HCHO data are averaged over the time during which the TOGA-TOF  
287 sampling occurred. Here we use two averaging methods for HCHO comparison: (1) normal  
288 averaging and (2) volume-weighted averaging. The normal averaging is performed by taking the  
289 arithmetic mean of the 1-Hz source data measured between the start and stop times of TOGA-  
290 TOF sampling. Below LLOD values of the source data are included in the averaging. A minimum  
291 of at least one valid (i.e., measured value or below LLOD) 1-Hz source data point during the  
292 TOGA-TOF sampling period is allowed for the analysis to produce a non-missing merged value.  
293 This algorithm is how the NASA online merging tool generates the TOGA.DC8\_MRG and is  
294 publicly available on the NASA Langley Research Center (LaRC) Airborne Science Data  
295 repository at [https://www-air.larc.nasa.gov/cgi-](https://www-air.larc.nasa.gov/cgi-bin/ArcView/firexaq?MERGE=1#TOGA.DC8_MRG/)  
296 [bin/ArcView/firexaq?MERGE=1#TOGA.DC8\\_MRG/](https://www-air.larc.nasa.gov/cgi-bin/ArcView/firexaq?MERGE=1#TOGA.DC8_MRG/). More details on the NASA online merging  
297 tool can be found in <https://www-air.larc.nasa.gov/missions/etc/onlinemergedoc.pdf>.

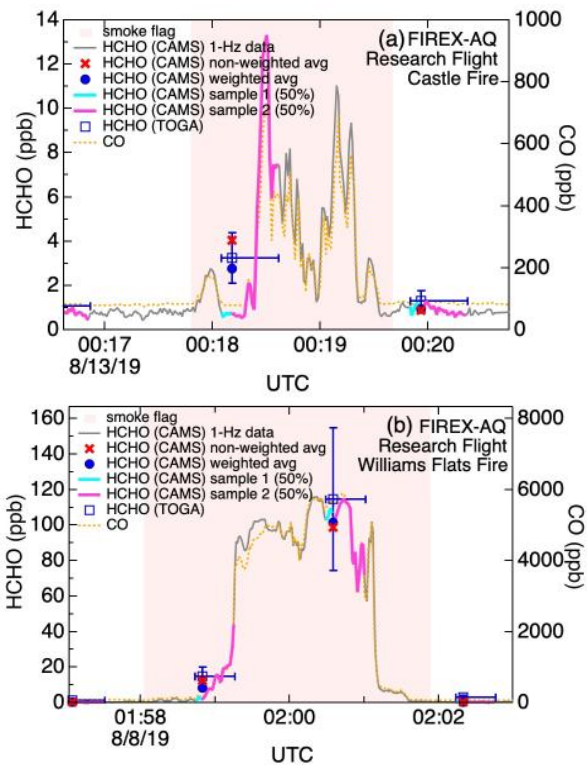


**Figure 3.** Example time series of [ISAF-CAMS](#) and TOGA-TOF HCHO and LGR CO observations during FIREX-AQ transverse (i.e., perpendicular to the transport of the fire plume) plume transects with relatively (a) high and (b) low variability in the observed 1-Hz HCHO. The pink shading shows when the DC-8 was inside the smoke plume based on the relative changes in CO. Vertical error bars on the TOGA-TOF HCHO data points show the measurement uncertainty ( $\pm 35\%$ ), centered on the TOGA-TOF sampling time midpoint, and the horizontal error bars span the start to stop times of each TOGA-TOF sample. For each of the start-to-midpoint and midpoint-to-stop times of the TOGA-TOF sampling periods, 50% of the total sample volume occurred. These times (start/midpoint/stop) were used for deriving weighted averages of the 1-Hz HCHO and CO data.

The second averaging method is the volume-weighted averaging method based on the volume of air sampled. [A post-mission laboratory analysis of the normalized volume vs. sample collection duration demonstrated that the flow rate through the sample trap was not constant during the sampling time period, despite the mass flow controller \(MFC\) being set to a fixed value. Specifically, relative flow rates were higher during the initial seconds of sampling before](#)

317 ~~decreasing to the MFC setpoint. Through a series of experiments, we quantified the total sample~~  
318 ~~volume as a function of collection time and derived an empirical relationship to determine the~~  
319 ~~sample-volume midpoint, defined as the time at which 50% of the total collected volume had been~~  
320 ~~accumulated during the sampling cycle (Fig. 3). Midpoints were calculated for each sample using~~  
321 ~~this method. During TOGA-TOF sampling, the flow rate through the sample trap was variable,~~  
322 ~~with faster relative flow rates at the beginning of each sample. We define a midpoint, as shown in~~  
323 ~~Fig. 3, at which the sample volume reached 50% of the total volume during the corresponding~~  
324 ~~sampling cycle. The midpoint is calculated for each sample by determining the total sample~~  
325 ~~volume collected for samples with varying sampling durations, and then the relationship between~~  
326 ~~the total sampling time and the sample volume to determine the time at which half the sample~~  
327 ~~volume was collected.~~ The midpoints determined through this method are reported in the TOGA-  
328 TOF FIREX-AQ data files archived at the NASA Atmospheric Science Data Center (ASDC)  
329 ([https://doi.org/10.5067/ASDC/FIREXAQ\\_TraceGas\\_AircraftInSitu\\_DC8\\_Data\\_1](https://doi.org/10.5067/ASDC/FIREXAQ_TraceGas_AircraftInSitu_DC8_Data_1)). The  
330 arithmetic mean of the 1-Hz data is thus calculated for the time periods between the start to  
331 midpoint ( $T_1$ ) and midpoint to stop times ( $T_2$ ), and these two means are averaged to weight the  
332 merge value on the sampled volume.

333 When sampling near strong VOC sources (e.g., wildfires or urban emissions), air masses  
334 often have significant heterogeneity of HCHO levels from varying direct emissions and  
335 photochemical production from rapidly changing VOC precursors. In those cases, using the non-  
336 weighted averages of 1-Hz measurements can lead to significant biases when they are directly  
337 compared to the TOGA-TOF data. Therefore, using volume-weighted averages of higher-  
338 frequency data that factor in the true sample volume midpoints for comparisons with TOGA-TOF  
339 data allows a more accurate comparison of the sampled air masses.

340 Using the above methodology, volume-weighted averages of LGR and DACOM 1-Hz CO  
341 data are carried out, during the times when TOGA was sampling. In our study, we use the volume-  
342 weighted averaged LGR CO data when it is available, and for times when it is not available, we  
343 use the volume-weighted averaged DACOM CO data multiplied by 0.978 to account for the  
344 relative differences in the two CO datasets. We normalized to the LGR CO data as it is a little  
345 lower to be conservative in our analyses, although the two CO datasets are in excellent agreement  
346 (Fig. S4) and within the combined measurement uncertainties ( $LGR = 2 \text{ ppb} + 2\%$  for LGR, and  
347  $DACOM = \text{typically } \pm 2\%$  for DACOM).

#### 348 2.4 Formaldehyde Normalized Excess Mixing Ratios

349 We compare HCHO normalized excess mixing ratios (NEMRs) for Western U.S. wildland  
350 fires calculated using HCHO reported by TOGA-TOF, ISAF, and CAMS. There are several ways  
351 to derive NEMRs (Yokelson et al., 2013a) and here we used the slope method, which involves  
352 determining the slope of HCHO in ppt against CO in ppb for a single plume transect and the  
353 background air outside the plume. CO was used as the reference species to normalize for dilution  
354 as it is a conserved biomass burning tracer in wildfire plumes (Müller et al., 2016; Selimovic et  
355 al., 2019; Yokelson et al., 2013a). For the NEMRs from CAMS and ISAF, we use the 1-Hz HCHO  
356 and CO data for the entire plume transect. For the TOGA-TOF NEMRs, we use the discrete HCHO  
357 sampling points, which range between two and ten samples for each plume transect—including  
358 a background sample and plotted these against the volume-weighted average (described in Sect.  
359 2.3.4) TOGA merged CO for corresponding sampling periods.

360 The NEMR analysis was carried out for the plumes selected based on the following criteria:  
361 a) plume transects perpendicular to the fire source, b) availability of at least one full TOGA-TOF  
362 sampling cycle within the plume, c) stable background HCHO prior to and after the plume transect,

363 and d) availability of both CAMS and ISAF 1\_-Hz HCHO data sets and CO for both background  
364 and in-plume sampling. Fire plumes were identified via plume flags using above background CO  
365 in addition to visual inspection of the data (FIRE\_FLAG\_TABULAR\_DATA.dat, [https://www-  
366 air.larc.nasa.gov/cgi-bin/ArcView/firexaq#SCHWARZ.JOSHUA/](https://www-air.larc.nasa.gov/cgi-bin/ArcView/firexaq#SCHWARZ.JOSHUA/)). Based on these criteria,  
367 NEMRs were calculated for a total of 86 plume transects from 7 fire sources in the Western U.S.  
368 and these are summarized in the supporting information (**Table S1**).

### 369 **3. Results and Discussion**

#### 370 **3.1 Comparison of HCHO between different instrumental techniques**

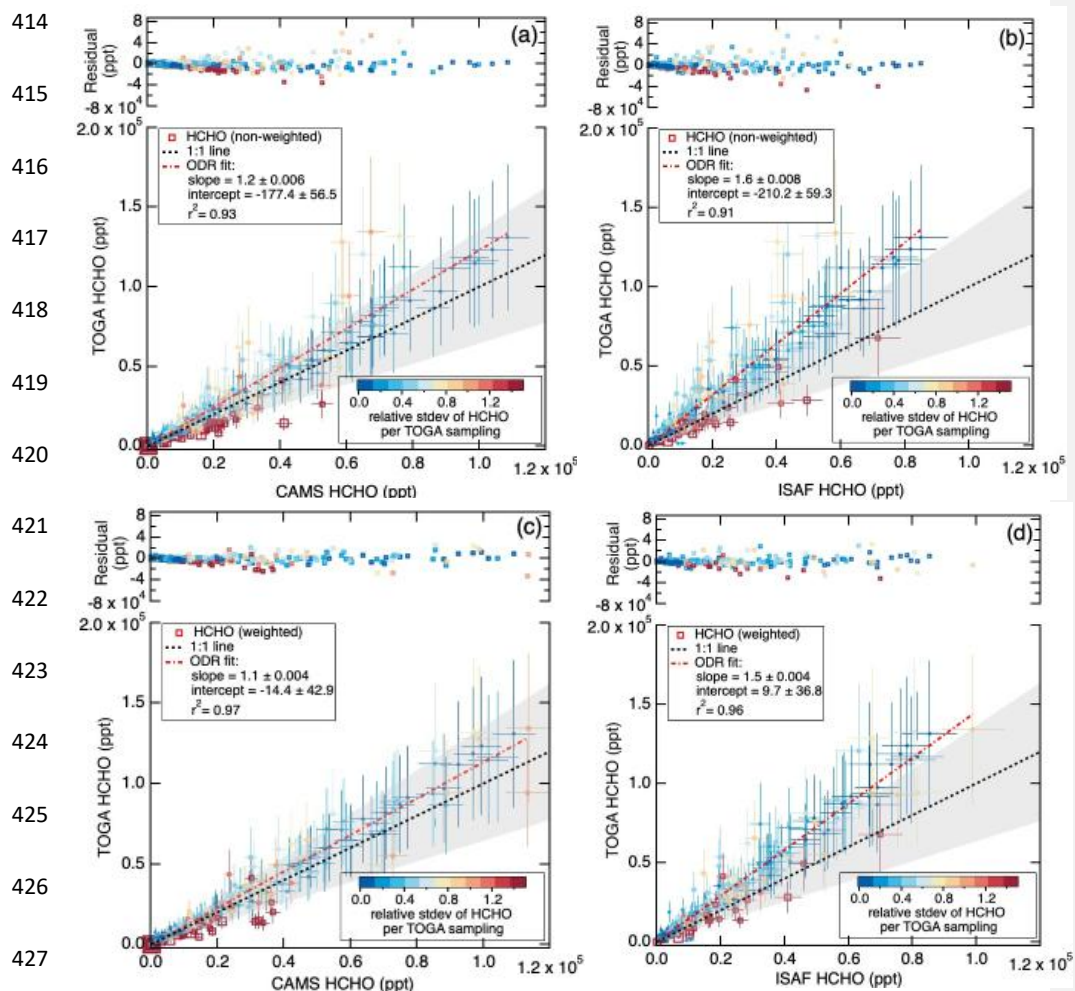
371 Direct intercomparisons of measured HCHO between TOGA-TOF and the 1\_-Hz  
372 instruments were carried out for data collected during all flights with available HCHO observations  
373 onboard the DC-8. This included 13 flights sampling Western U.S. fires, 7 flights in the  
374 Southeastern U.S., and 2 transit flights (**Fig. S1**). The dataset allowed comparisons of the widest  
375 possible range of HCHO observed in the troposphere (below 100 ppt to ~ 100 ppb). **Figure 4**  
376 shows correlations between TOGA-TOF, CAMS, and ISAF HCHO, averaged during the  
377 corresponding TOGA-TOF sampling periods. Comparisons with normal averaged 1\_-Hz HCHO  
378 (**Fig. 4a** and **b**) and volumed-weighted averaged 1\_-Hz HCHO (**Fig. 4c** and **b**), described in **Sect.**  
379 **2.3**, are both shown. The data points are colored according to the relative standard deviation of  
380 HCHO, calculated as the standard deviation of 1\_-Hz HCHO data during the TOGA-TOF sampling  
381 period divided by the HCHO measured by TOGA-TOF. This relative standard deviation represents  
382 the variability of the 1\_-Hz HCHO data during the TOGA-TOF sampling period.

383 Both non-weighted (**Fig. 4a**) and volume-weighted (**Fig. 4c**) averages showed that HCHO  
384 measured by CAMS was within the 35% measurement uncertainty of the TOGA-TOF while the  
385 comparisons with ISAF (**Fig. 4b** and **d**) were outside of the range of measurement uncertainties.

386 When using the non-weighted averaging method (**Fig. 4a** and **b**), the bivariate fitting (orthogonal  
387 distance regression, ODR) of the TOGA-TOF and the 1-Hz HCHO gave a slope of 1.2 for CAMS  
388 ( $y$ -intercept -177.4 ppt, **Fig. 4a**) and 1.6 for ISAF ( $y$ -intercept -210.2 ppt, **Fig. 4b**). The  $y$ -axis  
389 residuals from the ODR fit were largest for data points with higher relative standard deviations  
390 (i.e.,  $> 0.7$ ) of HCHO. For the non-weighted averages, the absolute values of the  $y$ -axis residuals  
391 ranged from 0.6 ppt to 59.0 ppb for CAMS (mean  $\pm$  standard deviation =  $1.0 \pm 3.0$  ppb) and 0.1  
392 ppt to 68.1 ppb for ISAF ( $0.9 \pm 3.2$  ppb). To differentiate the dependence on HCHO variations  
393 during each TOGA-TOF sampling, a relative standard deviation of 0.7 was used as a cut-off  
394 threshold. For data points with relative standard deviations  $> 0.7$ , residuals ranged from 2.6 ppt to  
395 59.0 ppb ( $2.7 \pm 6.8$  ppb) for CAMS and 52.1 ppt to 46.8 ppb ( $3.7 \pm 7.8$  ppb) for ISAF. In  
396 comparison, for less heterogeneous air masses (i.e., TOGA-merge 1-Hz HCHO with relative  
397 standard deviations  $< 0.7$ ), residuals ranged from 0.6 ppt to 44.1 ppb ( $0.7 \pm 1.8$  ppb) for CAMS  
398 and from 0.1 ppt to 68.1 ppb ( $0.6 \pm 2.5$  ppb) for ISAF. Therefore, the data points with less variable  
399 HCHO (i.e., HCHO relative standard deviation  $< 0.7$ ) showed on average a factor of 4–6 lower  
400 residual values, showing that the increased heterogeneity of HCHO in the sampled air masses lead  
401 to poorer correlations between TOGA-TOF and the 1-Hz HCHO instruments.

402 For more accurate comparisons, the CAMS and ISAF HCHO data averages were weighted  
403 by the TOGA-TOF sampling volume, factoring in the 50% volume sampling midpoint. Weighted  
404 averages of the CAMS and ISAF measured HCHO improved the correlations with TOGA-TOF to  
405 give an  $r^2$  of 0.97 (compared to 0.93 for non-weighted averages) for CAMS and 0.96 (compared  
406 to 0.91 for non-weighted averages) for ISAF (**Fig. 4c** and **d**). The residuals of the volume-weighted  
407 averages were 30% lower for CAMS (range 0.2 ppt to 32.2 ppb and average  $0.7 \pm 2.0$  ppb) and  
408 33% lower for ISAF (range 0.03 ppt to 32 ppb and average  $0.6 \pm 2.0$  ppb). Biases at low mixing

409 ratios significantly improved when using volume-weighted averages with absolute values of the  
410 y-intercepts much closer to 0 than the non-weighted averages, at  $-14.4 \pm 42.9$  ppt for CAMS  
411 (versus  $-177.4 \pm 56.4$  ppt) and  $9.7 \pm 36.8$  ppt for ISAF (versus  $-210.2 \pm 59.3$  ppt). Comparisons  
412 between TOGA-TOF and the UiO PTR-ToF-MS (**Fig. S5**), showed similar results with better  
413 agreement when using volume-weighted averages.



428 **Figure 4.** Correlation of measured HCHO (a,c) between TOGA-TOF and CAMS and (b,d) between TOGA-TOF  
 429 and ISAF. CAMS and ISAF 1-Hz HCHO data were averaged over the TOGA-TOF sampling start and stop times  
 430 using the (a,b) non-weighted and (c,d) volume-weighted averaging methods. Measurement uncertainties of each  
 measurement technique are shown as error bars. The grey shading around the 1:1 line is the HCHO measurement  
 uncertainties of the two corresponding instruments added in quadrature. Each data point is colored by the relative  
 standard deviation of the 1-Hz HCHO data (standard deviation of 1-Hz averaged HCHO divided by TOGA-TOF  
 HCHO) during the TOGA-TOF sampling period.

431 The discrepancies of HCHO between different measurement techniques during FIREX-  
 432 AQ are similar to those shown by Liao et al. (2021), in which a comparison of CAMS vs. ISAF

433 HCHO data had a slope of 1.27. In our study, a comparison of the volume-weighted TOGA-merge  
434 CAMS vs. ISAF HCHO from FIREX-AQ has a slope of 1.28, similar to Liao et al. (2021). The  
435 minor difference in the slopes is most likely due to the different periods of data selected for analysis  
436 as we only included CAMS and ISAF data during TOGA sampling in our analysis. Liao et al.  
437 (2021) suggested that the main discrepancies between CAMS and ISAF were driven by the  
438 uncertainties in the absolute calibration of the HCHO standards. As mentioned in **Sect. 2.2**, each  
439 HCHO measurement technique has been carefully calibrated with HCHO standards. The HCHO  
440 calibration standards used by each group were gravimetrically prepared and the absolute  
441 concentrations were quantified using optical absorption techniques. As the main purpose of this  
442 paper is to validate the TOGA-TOF as a unique technique for measuring HCHO, we will not  
443 further explore the reasons for the discrepancies between the instruments.

### 444 **3.2 Comparison of HCHO NEMR between different instrumental techniques**

445 Normalized excess mixing ratios (NEMR) are used to derive the enhancement of a trace  
446 gas within a smoke plume (Yokelson et al., 2013a). **Figure 5** shows HCHO NEMRs derived from  
447 Western U.S. fires using the TOGA-TOF, CAMS, and ISAF instrumental techniques with respect  
448 to smoke plume physical age ([https://www-air.larc.nasa.gov/cgi-  
449 bin/ArcView/firexaq#SCHWARZ.JOSHUA/](https://www-air.larc.nasa.gov/cgi-bin/ArcView/firexaq#SCHWARZ.JOSHUA/)). Based on the instrument uncertainties of both CO  
450 and the individual HCHO measurements, the uncertainties of the NEMRs are 35%, 6%, and 10%  
451 for TOGA-TOF, CAMS, and ISAF, respectively. The HCHO NEMRs observed during FIREX-  
452 AQ from TOGA-TOF were in the range of 12 to 30 ppt ppb<sup>-1</sup> CO. These NEMRs were within the  
453 wide range observed from previous wildfire biomass burning studies from 2.2 to 46 ppt ppb<sup>-1</sup> CO  
454 (e.g., Hornbrook et al., 2011 and references therein) and during prescribed burning events in the  
455 Southeastern U.S. during FIREX-AQ that ranged from 16 to 29 ppt ppb<sup>-1</sup> CO (Travis et al., 2023).

456 The quadratic polynomial fitting of HCHO NEMRs from all three instruments showed that the  
457 NEMRs increased up to ~ 5 h of plume physical age then declined. The age at which the HCHO  
458 NEMRs from each instrument begin to decrease (i.e., the change in the NEMRs with respect to  
459 plume age = 0) are all within 20 minutes of 5 h. This trend with respect to plume physical age  
460 agrees with what Liao et al. (2021) reported for HCHO NEMRs measured by ISAF from individual  
461 fire sources and is driven by the balance of production of HCHO, mainly from VOC oxidation by  
462 OH, and loss of HCHO, mainly from photolysis, throughout the aging of plume (Liao et al., 2021).

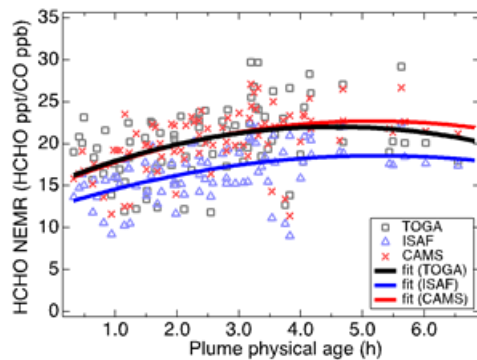
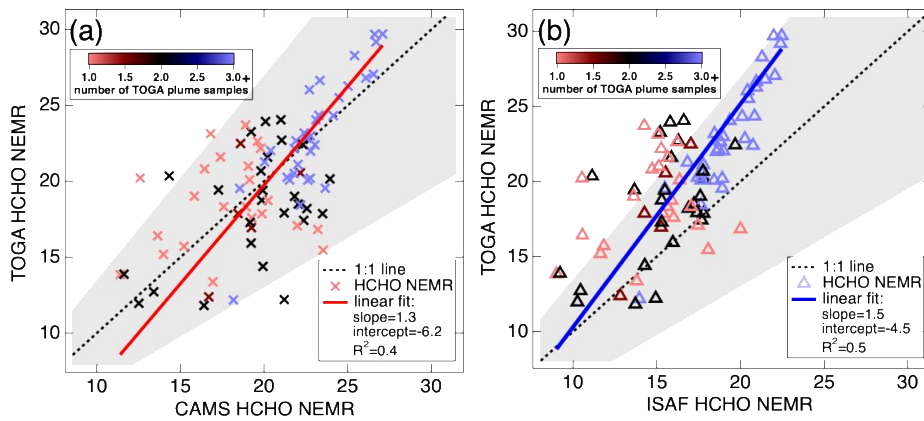


**Figure 5.** HCHO NEMRs of Western U.S. fires with respect to plume physical age during FIREX-AQ. Quadratic polynomial fittings of NEMRs derived using TOGA-TOF, CAMS, and ISAF HCHO data are shown.

463

464 While the trend with respect to plume physical age was similar using HCHO from the  
465 different instruments, systematic differences were observed. To further investigate the possibility  
466 of systematic differences of the NEMRs derived from the three HCHO instruments, paired *t*-tests  
467 were used as a statistical method to compare two different analytical methods (Yen et al., 2020).  
468 Here we carried out a paired *t*-test on the HCHO NEMRs calculated from the HCHO  
469 measurements from the TOGA-TOF against CAMS and ISAF data. The sample number of the  
470 analysis was equivalent to the number of selected transects for NEMR analysis (86 pairs). The null

471 hypothesis was whether the HCHO NEMRs from a pair of instruments are the same ( $H_0: \mu_1 = \mu_2$ )  
 472  $= f_2$ ), where the absolute value of the  $t$ -value ( $t$ ) higher than the critical  $t$  ( $T_c$ ) rejects the hypothesis.  
 473 Between the TOGA-TOF and CAMS NEMRs, the analysis yielded  $t = -0.42$ ,  $T_c = 1.99$ , and  $p$ -  
 474 value = 0.68, retaining the hypothesis (at the  $p = 0.05$  (5%) level). Between the TOGA-TOF and  
 475 ISAF NEMRs, the analysis yielded  $t = 11.53$ ,  $T_c = 1.99$ , and  $p$ -value =  $4.68 \times 10^{-19}$ , rejecting the  
 476 hypothesis. Between the CAMS and ISAF NEMRs, the analysis yielded  $t = 29.84$ ,  $T_c = 1.99$ , and  
 477  $p$ -value =  $8.21 \times 10^{-47}$ , again rejecting the hypothesis. Therefore, both TOGA-TOF and CAMS  
 478 derived NEMRs had a systematic difference from the ISAF derived NEMRs with a significance at  
 479 the  $p = 0.05$  (5%) level.



480 **Figure 6.** Correlation plots between (a) TOGA-TOF and CAMS and (b) TOGA-TOF and ISAF derived HCHO  
 481 NEMRs. Orthogonal distance regression fittings of the correlations are shown. The grey shading around the  
 482 dashed 1:1 line shows the measurement uncertainty (35%) of TOGA-TOF HCHO.

481 As mentioned in **Sect. 3.1**, systematic biases exist between the HCHO measurement  
 482 techniques which are likely due to calibration standard differences. As illustrated in **Fig. 5**, these  
 483 biases are similarly present in the derived HCHO NEMRs. Nonetheless, comparisons between the

484 HCHO NEMRs derived from TOGA-TOF and CAMS (Fig. 6a) and TOGA-TOF and ISAF (Fig.  
485 6b) indicate that the correlations are within the uncertainty bounds of the NEMR.

### 486 3.3 Discussion on TOGA-TOF HCHO NEMRs and their applicability

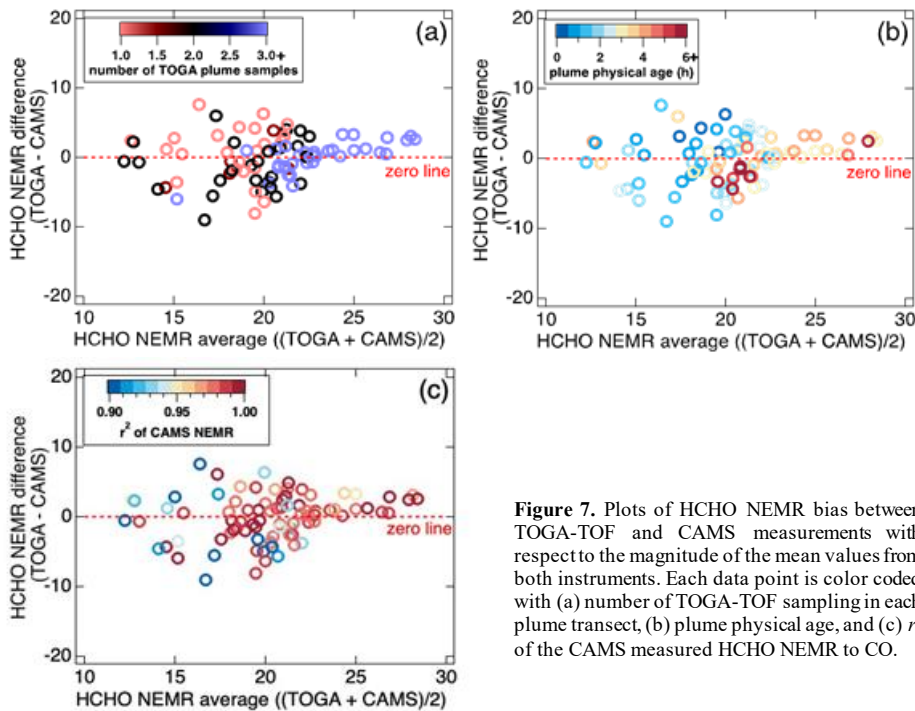


Figure 7. Plots of HCHO NEMR bias between TOGA-TOF and CAMS measurements with respect to the magnitude of the mean values from both instruments. Each data point is color coded with (a) number of TOGA-TOF sampling in each plume transect, (b) plume physical age, and (c)  $r^2$  of the CAMS measured HCHO NEMR to CO.

487  
488 The applicability of TOGA-TOF-derived HCHO NEMRs is further explored for different  
489 smoke plume conditions. Figure 7 shows the difference of HCHO NEMRs between TOGA-TOF  
490 and CAMS with respect to the averages from the two methods. Similar to Fig. 5, Fig. 7b shows  
491 that the averaged HCHO NEMRs increase with plume physical age. With greater plume physical  
492 age, the bias between TOGA-TOF driven HCHO NEMRs to CAMS becomes lower (Fig. 7b) and  
493 this lower bias corresponds to more TOGA-TOF samples at each plume transect (Fig. 7a). With

494 increasing physical age, the smoke plumes studied were generally more dispersed and spatially  
495 wider, therefore allowing more TOGA-TOF samples per transect.

496 The reduced bias between the two instrumental techniques with plume physical age can be  
497 explained from the ~~evolution-reduced~~ plume heterogeneity with aging, as indicated by the  
498 improved  $r^2$  of each plume sampling with plume physical age (**Fig. 7c**). Modeling studies of fire  
499 plumes (Trentmann et al., 2003a, 2003b; Wang et al., 2021) have shown significant spatial  
500 heterogeneity, both vertically and horizontally, of fire plumes with different levels of oxidants (i.e.,  
501 OH, O<sub>3</sub>, NO<sub>3</sub>). This plume heterogeneity has also been observed in power plant plumes (Brock et  
502 al., 2002). As discussed in Wang et al. (2021), at the early stage of a fire plume, OH levels are  
503 severely dampened at the core of the plume, mainly due to attenuation of solar radiation from  
504 aerosols, but enhanced at the edges. With aging of the plume, OH levels become more  
505 homogeneous (Wang et al., 2021). Liao et al. (2021) showed that HCHO levels observed in fire  
506 plumes as they age during FIREX-AQ were primary emissions coupled with subsequent photolytic  
507 loss and secondary production, primarily from the oxidation of VOCs with OH. Therefore, with  
508 plume physical age, as oxidant levels and photochemistry become more homogeneous, we can  
509 expect HCHO NEMRs to be more constant throughout a transect perpendicular to the direction of  
510 the smoke transport. As such, the  $r^2$  value of the slope of CAMS HCHO and CO, from which the  
511 NEMRs were calculated, is closer to 1 for larger NEMRs (and larger plume physical ages) (**Fig.**  
512 **7c**). These results demonstrate that the TOGA-TOF data are sufficient for assessing HCHO  
513 NEMRs in plumes with physical ages > 2–3 h and may result in a small bias in calculated NEMRs  
514 for younger, narrower plumes in comparison to those derived using fast HCHO measurement  
515 techniques.

#### 516 4. Conclusions

517 In this study, we demonstrated the TOGA-TOF as a fast response (< 2 min) GC/MS  
518 instrument that can measure HCHO along with > 100 additional C<sub>1</sub> to C<sub>10</sub> VOCs. During FIREX-  
519 AQ, the TOGA-TOF measured a wide range of HCHO mixing ratios with an LLOD of 20 ppt  
520 aboard the NASA DC-8. To our knowledge, this technique has not been previously reported for  
521 any ambient measurements. The discrete TOGA-TOF HCHO measurements during FIREX-AQ  
522 are comparable to the averaged non-discrete 1-Hz HCHO data measured by the CAMS and UiO  
523 PTR-ToF-MS instruments while the discrepancies are beyond the combined instrumental  
524 uncertainties for the TOGA-TOF and ISAF instruments. The discrepancies between HCHO  
525 instrumental techniques during FIREX-AQ are currently believed to be due to differences in  
526 calibration standards as quantified by different optical techniques. Using volume-weighted TOGA  
527 merge averages of HCHO measured by CAMS, ISAF, and UiO PTR-ToF-MS improved the  
528 comparison agreement with TOGA-TOF HCHO observations. Therefore, we strongly encourage  
529 the community to use the reported Time\_Start, Time\_Mid, and Time\_Stop values in the TOGA-  
530 TOF archived data files to determine volume-weighted averages of concurrent measurements.

531 TOGA-TOF derived NEMRs showed similar trends with plume physical age to what has  
532 been reported from ISAF (Liao et al., 2021), with NEMRs increasing with plume ages up to ~ 5 h.  
533 Due to its nature of taking discrete subsamples of air masses, [as shown in Fig. 3a, highly](#)  
534 [heterogeneous features may not be captured by the TOGA-TOF systems](#)~~small biases may remain~~  
535 in comparison to fast HCHO measurement techniques, especially [in chemically dynamic](#)  
536 [environments near](#)~~near~~ strong sources with highly heterogeneous emissions and rapidly varying  
537 HCHO production and loss [often detected during airborne measurements](#). Nevertheless, the  
538 technique used in the TOGA-TOF offers a powerful HCHO-measuring method to the scientific  
539 community, with the capability to simultaneously measure > 100 other C<sub>1</sub>-C<sub>10</sub> VOC species. The

540 wide range of gas-phase VOCs measured with the TOGA-TOF can be used to provide significant  
541 insights into understanding the photochemical state of air masses in rural to polluted  
542 environments. In addition, [the time resolution and inherent averaging is well-suited for](#) ~~to~~  
543 verifying satellite observations, three-dimensional modeling, and to compare with other  
544 instrumental techniques.

545 **Data availability.** All data used in this paper are available at [https://www-](https://www-air.larc.nasa.gov/missions/firex-aq/index.html)  
546 [air.larc.nasa.gov/missions/firex-aq/index.html](https://www-air.larc.nasa.gov/missions/firex-aq/index.html)

547 **Author contributions.** ECA conceptualized the project. DJ performed the data analyses and wrote  
548 the manuscript with input from ECA and RSH, RSH, AJH, GD, HSH, JPD, AF, DK, JW, PW,  
549 TFH, GMW, JSC, JP, AW, TM, JBN, FP, JD, CW, JS, ECA performed the measurements, CDH  
550 analyzed the fire smoke ages, AS and EG contributed to the smoke and fuel identification data  
551 product, JHC was the project PI and provided guidance on the analyses.

552  
553 **Competing Interests.** The authors declare they have no conflict of interest. Some authors are  
554 members of the editorial board of AMT.

555  
556 **Acknowledgements.** The authors thank the entire FIREX-AQ Science Team and the NASA DC-8  
557 crew. The authors would also like to thank Hyeong-Ahn Kwon at the University of Suwon for  
558 discussions on HCHO satellite observations.

559  
560 **Financial Support.** Primary support for DJ for this project was provided by the NSF National  
561 Center for Atmospheric Research (NCAR) Advanced Study Program Postdoctoral Fellowship.  
562 This material is based upon work supported by the NSF National Center for Atmospheric  
563 Research, which is a major facility sponsored by the U.S. National Science Foundation under  
564 Cooperative Agreement No. 1852977. This research was also funded in part by NASA award No.  
565 80NSSC18K0633. Additional support was provided by NOAA's Cooperative Agreements with  
566 CIRES NA17OAR4320101 and NA22OAR4320151.

## 567 568 569 **References**

570 Akagi, S. K., Yokelson, R. J., Wiedinmyer, C., Alvarado, M. J., Reid, J. S., Karl, T., Crounse, J.  
571 D., and Wennberg, P. O.: Emission factors for open and domestic biomass burning for use in  
572 atmospheric models, *Atmos. Chem. Phys.*, 11, 4039–4072, [https://doi.org/10.5194/acp-11-4039-](https://doi.org/10.5194/acp-11-4039-2011)  
573 2011, 2011.

574 Anderson, D. C., Nicely, J. M., Wolfe, G. M., Hanisco, T. F., Salawitch, R. J., Canty, T. P.,  
575 Dickerson, R. R., Apel, E. C., Baidar, S., Bannan, T. J., Blake, N. J., Chen, D., Dix, B.,  
576 Fernandez, R. P., Hall, S. R., Hornbrook, R. S., Gregory Huey, L., Josse, B., Jöckel, P.,  
577 Kinnison, D. E., Koenig, T. K., Le Breton, M., Marécal, V., Morgenstern, O., Oman, L. D., Pan,  
578 L. L., Percival, C., Plummer, D., Revell, L. E., Rozanov, E., Saiz-Lopez, A., Stenke, A., Sudo,  
579 K., Tilmes, S., Ullmann, K., Volkamer, R., Weinheimer, A. J., and Zeng, G.: Formaldehyde in

580 the Tropical Western Pacific: Chemical Sources and Sinks, Convective Transport, and  
581 Representation in CAM-Chem and the CCMI Models, *J. Geophys. Res.-Atmos.*, 122, 11201–  
582 11226, <https://doi.org/10.1002/2016JD026121>, 2017.

583 Apel, E. C., Hornbrook, R. S., Hills, A. J., Blake, N. J., Barth, M. C., Weinheimer, A., Cantrell,  
584 C., Rutledge, S. A., Basarab, B., Crawford, J., Diskin, G., Homeyer, C. R., Campos, T., Flocke,  
585 F., Fried, A., Blake, D. R., Brune, W., Pollack, I., Peischl, J., Ryerson, T., Wennberg, P. O.,  
586 Crouse, J. D., Wisthaler, A., Mikoviny, T., Huey, G., Heikes, B., O’Sullivan, D., and Riemer,  
587 D. D.: Upper tropospheric ozone production from lightning NO<sub>x</sub>-impacted convection: Smoke  
588 ingestion case study from the DC3 campaign, *J. Geophys. Res.-Atmos.*, 120, 2505–2523,  
589 <https://doi.org/10.1002/2014JD022121>, 2015.

590 Bourgeois, I., Peischl, J., Neuman, J. A., Brown, S. S., Allen, H. M., Campuzano-Jost, P.,  
591 Coggon, M. M., DiGangi, J. P., Diskin, G. S., Gilman, J. B., Gkatzelis, G. I., Guo, H., Halliday,  
592 H. A., Hanisco, T. F., Holmes, C. D., Huey, L. G., Jimenez, J. L., Lamplugh, A. D., Lee, Y. R.,  
593 Lindaas, J., Moore, R. H., Nault, B. A., Nowak, J. B., Pagonis, D., Rickly, P. S., Robinson, M.  
594 A., Rollins, A. W., Selimovic, V., St. Clair, J. M., Tanner, D., Vasquez, K. T., Veres, P. R.,  
595 Warneke, C., Wennberg, P. O., Washenfelder, R. A., Wiggins, E. B., Womack, C. C., Xu, L.,  
596 Zarzana, K. J., and Ryerson, T. B.: Comparison of Airborne Measurements of NO, NO<sub>2</sub>, HONO,  
597 NO<sub>y</sub>, and CO during FIREX-AQ, *Atmos. Meas. Tech.*, 15, 4901–4930,  
598 <https://doi.org/10.5194/amt-15-4901-2022>, 2022.

599 Brock, C. A., Washenfelder, R. A., Trainer, M., Ryerson, T. B., Wilson, J. C., Reeves, J. M.,  
600 Huey, L. G., Holloway, J. S., Parrish, D. D., Hübler, G., and Fehsenfeld, F. C.: Particle growth in  
601 the plumes of coal-fired power plants, *J. Geophys. Res.-Atmos.*, 107,  
602 <https://doi.org/10.1029/2001jd001062>, 2002.

603 Cao, H., Fu, T. M., Zhang, L., Henze, D. K., Miller, C. C., Lerot, C., Abad, G. G., De Smedt, I.,  
604 Zhang, Q., Van Roozendaal, M., Hendrick, F., Chance, K., Li, J., Zheng, J., and Zhao, Y.:  
605 Adjoint inversion of Chinese non-methane volatile organic compound emissions using space-  
606 based observations of formaldehyde and glyoxal, *Atmos. Chem. Phys.*, 18, 15017–15046,  
607 <https://doi.org/10.5194/acp-18-15017-2018>, 2018.

608 Cazorla, M., Wolfe, G. M., Bailey, S. A., Swanson, A. K., Arkinson, H. L., and Hanisco, T. F.: A  
609 new airborne laser-induced fluorescence instrument for in situ detection of formaldehyde  
610 throughout the troposphere and lower stratosphere, *Atmos. Meas. Tech.*, 8, 541–552,  
611 <https://doi.org/10.5194/amt-8-541-2015>, 2015.

612 Chan Miller, C., Jacob, D. J., Marais, E. A., Yu, K., Travis, K. R., Kim, P. S., Fisher, J. A., Zhu,  
613 L., Wolfe, G. M., Hanisco, T. F., Keutsch, F. N., Kaiser, J., Min, K. E., Brown, S. S.,  
614 Washenfelder, R. A., González Abad, G., and Chance, K.: Glyoxal yield from isoprene oxidation  
615 and relation to formaldehyde: Chemical mechanism, constraints from SENEX aircraft  
616 observations, and interpretation of OMI satellite data, *Atmos. Chem. Phys.*, 17, 8725–8738,  
617 <https://doi.org/10.5194/acp-17-8725-2017>, 2017.

618 Clafin, M. S., Pagonis, D., Finewax, Z., Handschy, A. V., Day, D. A., Brown, W. L., Jayne, J.  
619 T., Worsnop, D. R., Jimenez, J. L., Ziemann, P. J., de Gouw, J., and Lerner, B. M.: An in situ gas  
620 chromatograph with automatic detector switching between PTR-and EI-TOF-MS: Isomer-  
621 resolved measurements of indoor air, *Atmos. Meas. Tech.*, 14, 133–152,  
622 <https://doi.org/10.5194/amt-14-133-2021>, 2021.

623 Curci, G., Palmer, P. I., Kurosu, T. P., Chance, K., and Visconti, G.: Estimating European  
624 volatile organic compound emissions using satellite observations of formaldehyde from the  
625 Ozone Monitoring Instrument, *Atmos. Chem. Phys.*, 10, 11501–11517,  
626 <https://doi.org/10.5194/acp-10-11501-2010>, 2010.

627 Decker, Z. C. J., Robinson, M. A., Barsanti, K. C., Bourgeois, I., Coggon, M. M., Digangi, J. P.,  
628 Diskin, G. S., Flocke, F. M., Franchin, A., Fredrickson, C. D., Gkatzelis, G. I., Hall, S. R.,  
629 Halliday, H., Holmes, C. D., Huey, L. G., Lee, Y. R., Lindaas, J., Middlebrook, A. M., Montzka,  
630 D. D., Moore, R., Neuman, J. A., Nowak, J. B., Palm, B. B., Peischl, J., Piel, F., Rickly, P. S.,  
631 Rollins, A. W., Ryerson, T. B., Schwantes, R. H., Sekimoto, K., Thornhill, L., Thornton, J. A.,  
632 Tyndall, G. S., Ullmann, K., Van Rooy, P., Veres, P. R., Warneke, C., Washenfelder, R. A.,  
633 Weinheimer, A. J., Wiggins, E., Winstead, E., Wisthaler, A., Womack, C., and Brown, S. S.:  
634 Nighttime and daytime dark oxidation chemistry in wildfire plumes: An observation and model  
635 analysis of FIREX-AQ aircraft data, *Atmos. Chem. Phys.*, 21, 16293–16317,  
636 <https://doi.org/10.5194/acp-21-16293-2021>, 2021.

637 Duncan, B. N., Yoshida, Y., Olson, J. R., Sillman, S., Martin, R. V., Lamsal, L., Hu, Y.,  
638 Pickering, K. E., Retscher, C., Allen, D. J., and Crawford, J. H.: Application of OMI  
639 observations to a space-based indicator of NO<sub>x</sub> and VOC controls on surface ozone formation,  
640 *Atmos. Environ.*, 44, 2213–2223, <https://doi.org/10.1016/j.atmosenv.2010.03.010>, 2010.

641 Fried, A., Walega, J., Weibring, P., Richter, D., Simpson, I. J., Blake, D. R., Blake, N. J.,  
642 Meinardi, S., Barletta, B., Hughes, S. C., Crawford, J. H., Diskin, G., Barrick, J., Hair, J., Fenn,  
643 M., Wisthaler, A., Mikoviny, T., Woo, J.-H., Park, M., Kim, J., Min, K.-E., Jeong, S., Wennberg,  
644 P. O., Kim, M. J., Crounse, J. D., Teng, A. P., Bennett, R., Yang-Martin, M., Shook, M. A.,  
645 Huey, G., Tanner, D., Knote, C., Kim, J., Park, R., and Brune, W.: Airborne formaldehyde and  
646 volatile organic compound measurements over the Daesan petrochemical complex on Korea's  
647 northwest coast during the Korea-United States Air Quality study, *Elem. Sci. Anth.*, 8, 121,  
648 <https://doi.org/10.1525/elementa.2020.121>, 2020.

649 Gilman, J. B., Lerner, B. M., Kuster, W. C., Goldan, P. D., Warneke, C., Veres, P. R., Roberts, J.  
650 M., de Gouw, J. A., Burling, I. R., and Yokelson, R. J.: Biomass burning emissions and potential  
651 air quality impacts of volatile organic compounds and other trace gases from fuels common in  
652 the US, *Atmos. Chem. Phys.*, 15, 13915–13938, <https://doi.org/10.5194/acp-15-13915-2015>,  
653 2015.

654 Gilpin, T., Apel, E., Fried, A., Wert, B., Calvert, J., Genfa, Z., Dasgupta, P., Harder, J. W.,  
655 Heikes, B., Hopkins, B., Westberg, H., Kleindienst, T., Lee, Y. N., Zhou, X., Lonneman, W., and  
656 Sewell, S.: Intercomparison of six ambient [CH<sub>2</sub>O] measurement techniques, *J. Geophys. Res.-*  
657 *Atmos.*, 102, 21161–21188, <https://doi.org/10.1029/97jd01314>, 1997.

658 Gkatzelis, G. I., Coggon, M. M., Stockwell, C. E., Hornbrook, R. S., Allen, H., Apel, E. C., Bela,  
659 M. M., Blake, D. R., Bourgeois, I., Brown, S. S., Campuzano-Jost, P., Clair, J. M. S., Crawford,  
660 J. H., Crounse, J. D., Day, D. A., Digangi, J. P., Diskin, G. S., Fried, A., Gilman, J. B., Guo, H.,  
661 Hair, J. W., Halliday, H. S., Hanisco, T. F., Hannun, R., Hills, A., Huey, L. G., Jimenez, J. L.,  
662 Katich, J. M., Lamplugh, A., Lee, Y. R., Liao, J., Lindaas, J., Mckeen, S. A., Mikoviny, T.,  
663 Nault, B. A., Neuman, J. A., Nowak, J. B., Pagonis, D., Peischl, J., Perring, A. E., Piel, F.,  
664 Rickly, P. S., Robinson, M. A., Rollins, A. W., Ryerson, T. B., Schueneman, M. K., Schwantes,  
665 R. H., Schwarz, J. P., Sekimoto, K., Selimovic, V., Shingler, T., Tanner, D. J., Tomsche, L.,

666 Vasquez, K. T., Veres, P. R., Washenfelder, R., Weibring, P., Wennberg, P. O., Wisthaler, A.,  
667 Wolfe, G. M., Womack, C. C., Xu, L., Ball, K., Yokelson, R. J., and Warneke, C.:  
668 Parameterizations of US Wildfire and Prescribed Fire Emission Ratios and Emission Factors  
669 Based on FIREX-AQ Aircraft Measurements, *Atmos. Chem. Phys.*, 24, 929–956,  
670 <https://doi.org/10.5194/acp-24-929-2024>, 2024.

671 Green, J. R., Fiddler, M. N., Fibiger, D. L., McDuffie, E. E., Aquino, J., Campos, T., Shah, V.,  
672 Jaeglé, L., Thornton, J. A., DiGangi, J. P., Wolfe, G. M., Bililign, S., and Brown, S. S.:  
673 Wintertime Formaldehyde: Airborne Observations and Source Apportionment Over the Eastern  
674 United States, *J. Geophys. Res.-Atmos.*, 126, e2020JD033518,  
675 <https://doi.org/10.1029/2020JD033518>, 2021.

676 Hopkins, J. R., Still, T., Al-Haider, S., Fisher, I. R., Lewis, A. C., and Seakins, P. W.: A  
677 simplified apparatus for ambient formaldehyde detection via GC-pHID, *Atmos. Environ.*, 37,  
678 2557–2565, [https://doi.org/10.1016/S1352-2310\(03\)00178-X](https://doi.org/10.1016/S1352-2310(03)00178-X), 2003.

679 Hornbrook, R. S., Blake, D. R., Diskin, G. S., Fried, A., Fuelberg, H. E., Meinardi, S., Mikoviny,  
680 T., Richter, D., Sachse, G. W., Vay, S. A., Walega, J., Weibring, P., Weinheimer, A. J.,  
681 Wiedinmyer, C., Wisthaler, A., Hills, A., Riemer, D. D., and Apel, E. C.: Observations of  
682 nonmethane organic compounds during ARCTAS-Part 1: Biomass burning emissions and plume  
683 enhancements, *Atmos. Chem. Phys.*, 11, 11103–11130, [https://doi.org/10.5194/acp-11-11103-](https://doi.org/10.5194/acp-11-11103-2011)  
684 2011, 2011.

685 Hunter, M. C., Bartle, K. D., Seakins, P. W., and Lewis, A. C.: Direct measurement of  
686 atmospheric formaldehyde using gas chromatography-pulsed discharge ionisation detection,  
687 *Anal. Commun.*, 36, 101–104, <https://doi.org/10.1039/A809762C>, 1999.

688 Isaacman-VanWertz, G., Sueper, D. T., Aikin, K. C., Lerner, B. M., Gilman, J. B., de Gouw, J.  
689 A., Worsnop, D. R., and Goldstein, A. H.: Automated single-ion peak fitting as an efficient  
690 approach for analyzing complex chromatographic data, *J. Chromatogr. A*, 1529, 81–92,  
691 <https://doi.org/10.1016/j.chroma.2017.11.005>, 2017.

692 Jaeglé, L., Shah, V., Thornton, J. A., Lopez-Hilfiker, F. D., Lee, B. H., McDuffie, E. E., Fibiger,  
693 D., Brown, S. S., Veres, P., Sparks, T. L., Ebben, C. J., Wooldridge, P. J., Kenagy, H. S., Cohen,  
694 R. C., Weinheimer, A. J., Campos, T. L., Montzka, D. D., Digangi, J. P., Wolfe, G. M., Hanisco,  
695 T., Schroder, J. C., Campuzano-Jost, P., Day, D. A., Jimenez, J. L., Sullivan, A. P., Guo, H., and  
696 Weber, R. J.: Nitrogen Oxides Emissions, Chemistry, Deposition, and Export Over the Northeast  
697 United States During the WINTER Aircraft Campaign, *J. Geophys. Res.-Atmos.*, 123, 12368–  
698 12393, <https://doi.org/10.1029/2018JD029133>, 2018.

699 Kaiser, J., Jacob, D. J., Zhu, L., Travis, K. R., Fisher, J. A., González Abad, G., Zhang, L.,  
700 Zhang, X., Fried, A., Crounse, J. D., Clair, J. M. S., and Wisthaler, A.: High-resolution inversion  
701 of OMI formaldehyde columns to quantify isoprene emission on ecosystem-relevant scales:  
702 Application to the southeast US, *Atmos. Chem. Phys.*, 18, 5483–5497,  
703 <https://doi.org/10.5194/acp-18-5483-2018>, 2018.

704 [Karbiwnyk, C. M., Mills, C. S., Helmig, D., and Birks, J. W.: Use of Chlorofluorocarbons as](https://doi.org/10.1021/es025910q)  
705 [Internal Standards for the Measurement of Atmospheric Non-Methane Volatile Organic](https://doi.org/10.1021/es025910q)  
706 [Compounds Sampled onto Solid Adsorbent Cartridges, \*Environ. Sci. Technol.\*, 37, 1002–1007,](https://doi.org/10.1021/es025910q)  
707 <https://doi.org/10.1021/es025910q>, 2003.

708 Koss, A. R., Sekimoto, K., Gilman, J. B., Selimovic, V., Coggon, M. M., Zarzana, K. J., Yuan,  
709 B., Lerner, B. M., Brown, S. S., Jimenez, J. L., Krechmer, J., Roberts, J. M., Warneke, C.,  
710 Yokelson, R. J., and de Gouw, J.: Non-methane organic gas emissions from biomass burning:  
711 Identification, quantification, and emission factors from PTR-ToF during the FIREX 2016  
712 laboratory experiment, *Atmos. Chem. Phys.*, 18, 3299–3319, [https://doi.org/10.5194/acp-18-](https://doi.org/10.5194/acp-18-3299-2018)  
713 3299–2018, 2018.

714 Kwon, H. A., Park, R. J., Oak, Y. J., Nowlan, C. R., Janz, S. J., Kowalewski, M. G., Fried, A.,  
715 Walega, J., Bates, K. H., Choi, J., Blake, D. R., Wisthaler, A., and Woo, J. H.: Top-down  
716 estimates of anthropogenic VOC emissions in South Korea using formaldehyde vertical column  
717 densities from aircraft during the KORUS-AQ campaign, *Elem. Sci. Anth.*, 9, 00109,  
718 <https://doi.org/10.1525/elementa.2021.00109>, 2021.

719 Lee, M., Heikes, B. G., Jacob, D. J., Sachse, G., and Anderson, B.: Hydrogen peroxide, organic  
720 hydroperoxide, and formaldehyde as primary pollutants from biomass burning, *J. Geophys. Res.-*  
721 *Atmos.*, 102, 1301–1309, <https://doi.org/10.1029/96JD01709>, 1997.

722 Lerner, B. M., Gilman, J. B., Aikin, K. C., Atlas, E. L., Goldan, P. D., Graus, M., Hendershot,  
723 R., Isaacman-VanWertz, G. A., Koss, A., Kuster, W. C., Lueb, R. A., McLaughlin, R. J., Peischl,  
724 J., Sueper, D., Ryerson, T. B., Tokarek, T. W., Warneke, C., Yuan, B., and de Gouw, J. A.: An  
725 improved, automated whole air sampler and gas chromatography mass spectrometry analysis  
726 system for volatile organic compounds in the atmosphere, *Atmos. Meas. Tech.*, 10, 291–313,  
727 <https://doi.org/10.5194/amt-10-291-2017>, 2017.

728 Liao, J., Wolfe, G. M., Hannun, R. A., St. Clair, J. M., Hanisco, T. F., Gilman, J. B., Lamplugh,  
729 A., Selimovic, V., Diskin, G. S., Nowak, J. B., Halliday, H. S., Digangi, J. P., Hall, S. R.,  
730 Ullmann, K., Holmes, C. D., Fite, C. H., Agastra, A., Ryerson, T. B., Peischl, J., Bourgeois, I.,  
731 Warneke, C., Coggon, M. M., Gkatzelis, G. I., Sekimoto, K., Fried, A., Richter, D., Weibring, P.,  
732 Apel, E. C., Hornbrook, R. S., Brown, S. S., Womack, C. C., Robinson, M. A., Washenfelder, R.  
733 A., Veres, P. R., and Neuman, J. A.: Formaldehyde evolution in US wildfire plumes during the  
734 Fire Influence on Regional to Global Environments and Air Quality experiment (FIREX-AQ),  
735 *Atmos. Chem. Phys.*, 21, 18319–18331, <https://doi.org/10.5194/acp-21-18319-2021>, 2021.

736 Liao, J., Wolfe, G. M., Kotsakis, A. E., Nicely, J. M., St. Clair, J. M., Hanisco, T. F., Abad, G.  
737 G., Nowlan, C. R., Ayazpour, Z., De Smedt, I., Apel, E. C., Hornbrook, R. S.: Validation of  
738 formaldehyde products from three satellite retrievals (OMI SAO, OMPS-NPP SAO, and OMI  
739 BIRA) in the marine atmosphere with four seasons of Atmospheric Tomography Mission  
740 (ATom) aircraft observations, *Atmos. Meas. Tech.*, 18, 1–16, [https://doi.org/10.5194/amt-18-1-](https://doi.org/10.5194/amt-18-1-2025)  
741 2025, 2025.

742 Luecken, D. J., Hutzell, W. T., Strum, M. L., and Pouliot, G. A.: Regional sources of  
743 atmospheric formaldehyde and acetaldehyde, and implications for atmospheric modeling, *Atmos.*  
744 *Environ.*, 47, 477–490, <https://doi.org/10.1016/j.atmosenv.2011.10.005>, 2012.

745 Luecken, D. J., Napelenok, S. L., Strum, M., Scheffe, R., and Phillips, S.: Sensitivity of Ambient  
746 Atmospheric Formaldehyde and Ozone to Precursor Species and Source Types Across the  
747 United States, *Environ. Sci. Technol.*, 52, 4668–4675, <https://doi.org/10.1021/acs.est.7b05509>,  
748 2018.

749 Martin, R. V., Fiore, A. M., and Van Donkelaar, A.: Space-based diagnosis of surface ozone  
750 sensitivity to anthropogenic emissions, *Geophys. Res. Lett.*, 31, L06120,  
751 <https://doi.org/10.1029/2004GL019416>, 2004.

752 Müller, M., Mikoviny, T., Feil, S., Haidacher, S., Hanel, G., Hartungen, E., Jordan, A., Märk, L.,  
753 Mutschlechner, P., Schottkowsky, R., Sulzer, P., Crawford, J. H., and Wisthaler, A.: A compact  
754 PTR-ToF-MS instrument for airborne measurements of volatile organic compounds at high  
755 spatiotemporal resolution, *Atmos. Meas. Tech.*, 7, 3763–3772, <https://doi.org/10.5194/amt-7-3763-2014>, 2014.

757 Müller, M., Anderson, B. E., Beyersdorf, A. J., Crawford, J. H., Diskin, G. S., Eichler, P., Fried,  
758 A., Keutsch, F. N., Mikoviny, T., Thornhill, K. L., Walega, J. G., Weinheimer, A. J., Yang, M.,  
759 Yokelson, R. J., and Wisthaler, A.: In situ measurements and modeling of reactive trace gases in  
760 a small biomass burning plume, *Atmos. Chem. Phys.*, 16, 3813–3824,  
761 <https://doi.org/10.5194/acp-16-3813-2016>, 2016.

762 National Research Council (US) Committee on Toxicology: Formaldehyde - An Assessment of  
763 Its Health Effects, Washington (DC), 1980.

764 Nussbaumer, C. M., Crowley, J. N., Schuladen, J., Williams, J., Hafermann, S., Reiffs, A.,  
765 Axinte, R., Harder, H., Ernest, C., Novelli, A., Sala, K., Martinez, M., Mallik, C., Tomsche, L.,  
766 Plass-Dülmer, C., Bohn, B., Lelieveld, J., and Fischer, H.: Measurement report: Photochemical  
767 production and loss rates of formaldehyde and ozone across Europe, *Atmos. Chem. Phys.*, 21,  
768 18413–18432, <https://doi.org/10.5194/acp-21-18413-2021>, 2021.

769 Palmer, P. I., Jacob, D. J., Fiore, A. M., Martin, R. V., Chance, K., and Kurosu, T. P.: Mapping  
770 isoprene emissions over North America using formaldehyde column observations from space, *J.*  
771 *Geophys. Res.-Atmos.*, 108, 4180, <https://doi.org/10.1029/2002jd002153>, 2003.

772 Pfister, G., Wang, C. T., Barth, M., Flocke, F., Vizuete, W., and Walters, S.: Chemical  
773 Characteristics and Ozone Production in the Northern Colorado Front Range, *J. Geophys. Res.-*  
774 *Atmos.*, 124, 13397–13419, <https://doi.org/10.1029/2019JD030544>, 2019.

775 Possanzini, M., Palo, V. di, and Cecinato, A.: Sources and photodecomposition of formaldehyde  
776 and acetaldehyde in Rome ambient air, *Atmos. Environ.*, 36, 3195–3201,  
777 [https://doi.org/10.1016/S1352-2310\(02\)00192-9](https://doi.org/10.1016/S1352-2310(02)00192-9), 2002.

778 Rice, A. L. and Quay, P. D.: Isotopic analysis of atmospheric formaldehyde by gas  
779 chromatography isotope ratio mass spectrometry, *Anal. Chem.*, 78, 6320–6326,  
780 <https://doi.org/10.1021/ac0602367>, 2006.

781 Richter, D., Weibring, P., Walega, J. G., Fried, A., Spuler, S. M., and Taubman, M. S.: Compact  
782 highly sensitive multi-species airborne mid-IR spectrometer, *Appl. Phys. B*, 119, 119–131,  
783 <https://doi.org/10.1007/s00340-015-6038-8>, 2015.

784 Robinson, M. A., Decker, Z. C. J., Barsanti, K. C., Coggon, M. M., Flocke, F. M., Franchin, A.,  
785 Fredrickson, C. D., Gilman, J. B., Gkatzelis, G. I., Holmes, C. D., Lamplugh, A., Lavi, A.,  
786 Middlebrook, A. M., Montzka, D. M., Palm, B. B., Peischl, J., Pierce, B., Schwantes, R. H.,  
787 Sekimoto, K., Selimovic, V., Tyndall, G. S., Thornton, J. A., Van Rooy, P., Warneke, C.,  
788 Weinheimer, A. J., and Brown, S. S.: Variability and Time of Day Dependence of Ozone

789 Photochemistry in Western Wildfire Plumes, *Environ. Sci. Technol.*, 55, 10280–10290,  
790 <https://doi.org/10.1021/acs.est.1c01963>, 2021.

791 Sachse, G. W., Hill, G. F., Wade, L. O., and Perry, M. G.: Fast-response, high-precision carbon  
792 monoxide sensor using a tunable diode laser absorption technique, *J. Geophys. Res.-Atmos.*, 92,  
793 2071–2081, <https://doi.org/10.1029/JD092iD02p02071>, 1987.

794 Sagebiel, J. C., Zielinska, B., Pierson, W. R., and Gertler, A. W.: Real-world emissions and  
795 calculated reactivities of organic species from motor vehicles, *Atmos. Environ.*, 30, 2287–2296,  
796 [https://doi.org/10.1016/1352-2310\(95\)00117-4](https://doi.org/10.1016/1352-2310(95)00117-4), 1996.

797 Schroeder, J. R., Crawford, J. H., Fried, A., Walega, J., Weinheimer, A., Wisthaler, A., Müller,  
798 M., Mikoviny, T., Chen, G., Shook, M., Blake, D. R., and Tonnesen, G. S.: New insights into the  
799 column CH<sub>2</sub>O/NO<sub>2</sub> ratio as an indicator of near-surface ozone sensitivity, *J. Geophys. Res.-*  
800 *Atmos.*, 122, 8885–8907, <https://doi.org/10.1002/2017JD026781>, 2017.

801 Seinfeld, J. H. and Pandis, S. N.: *Atmospheric Chemistry and Physics: From Air Pollution to*  
802 *Climate Change*, 2nd ed., Wiley-Interscience, Hoboken, NJ, 2006.

803 Selimovic, V., Yokelson, R. J., McMeeking, G. R., and Coefield, S.: In situ measurements of  
804 trace gases, PM, and aerosol optical properties during the 2017 NW US wildfire smoke event,  
805 *Atmos. Chem. Phys.*, 19, 3905–3926, <https://doi.org/10.5194/acp-19-3905-2019>, 2019.

806 Sourì, A. H., Nowlan, C. R., Wolfe, G. M., Lamsal, L. N., Miller, C., González Abad, G., Janz,  
807 S. J., Fried, A., Blake, D. R., Weinheimer, A. J., Diskin, G. S., Liu, X., and Chance, K.:  
808 Revisiting the effectiveness of HCHO/NO<sub>2</sub> ratios for inferring ozone sensitivity to its precursors  
809 using high resolution airborne remote sensing observations in a high ozone episode during the  
810 KORUS-AQ campaign, *Atmos. Environ.*, 224, 117341,  
811 <https://doi.org/10.1016/j.atmosenv.2020.117341>, 2020.

812 Sourì, A. H., Johnson, M. S., Wolfe, G. M., Crawford, J. H., Fried, A., Wisthaler, A., Brune, W.  
813 H., Blake, D. R., Weinheimer, A. J., Verhoelst, T., Compernelle, S., Pinardi, G., Vigouroux, C.,  
814 Langerock, B., Choi, S., Lamsal, L., Zhu, L., Sun, S., Cohen, R. C., Min, K. E., Cho, C., Philip,  
815 S., Liu, X., and Chance, K.: Characterization of errors in satellite-based HCHO/NO<sub>2</sub>  
816 tropospheric column ratios with respect to chemistry, column-to-PBL translation, spatial  
817 representation, and retrieval uncertainties, *Atmos. Chem. Phys.*, 23, 1963–1986,  
818 <https://doi.org/10.5194/acp-23-1963-2023>, 2023.

819 Stavrakou, T., Müller, J.-F., De Smedt, I., Van Roozendael, M., van der Werf, G. R., Giglio, L.,  
820 and Guenther, A.: Evaluating the performance of pyrogenic and biogenic emission inventories  
821 against one decade of space-based formaldehyde columns, *Atmos. Chem. Phys.*, 1037–1060,  
822 <https://doi.org/10.5194/acp-9-1037-2009>, 2009.

823 Travis, K. R., Crawford, James. H., Soja, A. J., Gargulinski, E. M., Moore, R. H., Wiggins, E.  
824 B., Diskin, G. S., DiGangi, J. P., Nowak, J. B., Halliday, H., Yokelson, R. J., McCarty, J. L.,  
825 Simpson, I. J., Blake, D. R., Neinardi, S., Hornbrook, R. S., Apel, E. C., Hills, A. J., Warneke,  
826 C., Coggon, M. M., Rollins, A. W., Gilman, J. B., Womack, C. C., Robinson, M. A., Katich, J.  
827 M., Peischl, J., Gkatzelis, G. I., Bourgeois, I., Rickly, P. S., Lamplugh, A., Dibb, J. E., Jimenez,  
828 J. L., Campuzano-Jost, P., Day, D. A., Guo, H., Pagonis, D., Wennberg, P. O., Crouse, J. D.,  
829 Xu, L., Hanisco, T. F., Wolfe, G. M., Liao, J., St. Clair, J. M., Nault, B. A., Fried, A., and  
830 Perring, A. E.: Emission Factors for Crop Residue and Prescribed Fires in the Eastern US during

831 FIREX-AQ, *J. Geophys. Res.-Atmos.*, 128, e2023JD039309,  
832 <https://doi.org/10.1029/2023JD039309>, 2023.

833 Trentmann, J., Andreae, M. O., and Graf, H. F.: Chemical processes in a young biomass-burning  
834 plume, *J. Geophys. Res.-Atmos.*, 108, 4705, <https://doi.org/10.1029/2003jd003732>, 2003a.

835 Trentmann, J., Früh, B., Boucher, O., Trautmann, T., and Andreae, M. O.: Three-dimensional  
836 solar radiation effects on the actinic flux field in a biomass-burning plume, *J. Geophys. Res.-*  
837 *Atmos.*, 108, 4558, <https://doi.org/10.1029/2003jd003422>, 2003b.

838 Viskari, E.-L., Vartiainen, M., and Pasanen, P.: Seasonal and diurnal variation in formaldehyde  
839 and acetaldehyde concentrations along a highway in Eastern Finland, *Atmos. Environ.*, 34, 917–  
840 923, [https://doi.org/10.1016/S1352-2310\(99\)00307-6](https://doi.org/10.1016/S1352-2310(99)00307-6), 2000.

841 Wang, S., Coggon, M. M., Gkatzelis, G. I., Warneke, C., Bourgeois, I., Ryerson, T., Peischl, J.,  
842 Veres, P. R., Neuman, J. A., Hair, J., Shingler, T., Fenn, M., Diskin, G., Huey, L. G., Lee, Y. R.,  
843 Apel, E. C., Hornbrook, R. S., Hills, A. J., Hall, S. R., Ullmann, K., Bela, M. M., Trainer, M. K.,  
844 Kumar, R., Orlando, J. J., Flocke, F. M., and Emmons, L. K.: Chemical Tomography in a Fresh  
845 Wildland Fire Plume: A Large Eddy Simulation (LES) Study, *J. Geophys. Res.-Atmos.*, 126,  
846 e2021JD035203, <https://doi.org/10.1029/2021JD035203>, 2021.

847 Warneke, C., McKeen, S. A., de Gouw, J. A., Goldan, P. D., Kuster, W. C., Holloway, J. S.,  
848 Williams, E. J., Lerner, B. M., Parrish, D. D., Trainer, M., Fehsenfeld, F. C., Kato, S., Atlas, E.  
849 L., Baker, A., and Blake, D. R.: Determination of urban volatile organic compound emission  
850 ratios and comparison with an emissions database, *J. Geophys. Res.-Atmos.*, 112, D10S47,  
851 <https://doi.org/10.1029/2006JD007930>, 2007.

852 Warneke, C., Schwarz, J. P., Dibb, J., Kalashnikova, O., Frost, G., Al-Saad, J., Brown, S. S.,  
853 Brewer, Wm. A., Soja, A., Seidel, F. C., Washenfelder, R. A., Wiggins, E. B., Moore, R. H.,  
854 Anderson, B. E., Jordan, C., Yacovitch, T. I., Herndon, S. C., Liu, S., Kuwayama, T., Jaffe, D.,  
855 Johnston, N., Selimovic, V., Yokelson, R., Giles, D. M., Holben, B. N., Goloub, P., Popovici, I.,  
856 Trainer, M., Kumar, A., Pierce, R. B., Fahey, D., Roberts, J., Gargulinski, E. M., Peterson, D. A.,  
857 Ye, X., Thapa, L. H., Saide, P. E., Fite, C. H., Holmes, C. D., Wang, S., Coggon, M. M., Decker,  
858 Z. C. J., Stockwell, C. E., Xu, L., Gkatzelis, G., Aikin, K., Lefer, B., Kaspari, J., Griffin, D.,  
859 Zeng, L., Weber, R., Hastings, M., Chai, J., Wolfe, G. M., Hanisco, T. F., Liao, J., Campuzano  
860 Jost, P., Guo, H., Jimenez, J. L., Crawford, J., and Team, T. F.-A. S.: Fire Influence on Regional  
861 to Global Environments and Air Quality (FIREX-AQ), *J. Geophys. Res.-Atmos.*, 128,  
862 e2022JD037758, <https://doi.org/https://doi.org/10.1029/2022JD037758>, 2023.

863 Wolfe, G. M., Kaiser, J., Hanisco, T. F., Keutsch, F. N., de Gouw, J. A., Gilman, J. B., Graus,  
864 M., Hatch, C. D., Holloway, J., Horowitz, L. W., Lee, B. H., Lerner, B. M., Lopez-Hilifiker, F.,  
865 Mao, J., Marvin, M. R., Peischl, J., Pollack, I. B., Roberts, J. M., Ryerson, T. B., Thornton, J. A.,  
866 Veres, P. R., and Warneke, C.: Formaldehyde production from isoprene oxidation across NO<sub>x</sub>  
867 regimes, *Atmos. Chem. Phys.*, 16, 2597–2610, <https://doi.org/10.5194/acp-16-2597-2016>, 2016.

868 Yen, J., Leber, D., and Pibida, L.: Comparing Instruments, Gaithersburg, MD,  
869 <https://doi.org/10.6028/NIST.TN.2106>, 2020.

870 Yokelson, R. J., Andreae, M. O., and Akagi, S. K.: Pitfalls with the use of enhancement ratios or  
871 normalized excess mixing ratios measured in plumes to characterize pollution sources and aging,  
872 *Atmos. Meas. Tech.*, 6, 2155–2158, <https://doi.org/10.5194/amt-6-2155-2013>, 2013a.

873 Yokelson, R. J., Burling, I. R., Gilman, J. B., Warneke, C., Stockwell, C. E., de Gouw, J., Akagi,  
874 S. K., Urbanski, S. P., Veres, P., Roberts, J. M., Kuster, W. C., Reardon, J., Griffith, D. W. T.,  
875 Johnson, T. J., Hosseini, S., Miller, J. W., Cocker, D. R., Jung, H., and Weise, D. R.: Coupling  
876 field and laboratory measurements to estimate the emission factors of identified and unidentified  
877 trace gases for prescribed fires, *Atmos. Chem. Phys.*, 13, 89–116, [https://doi.org/10.5194/acp-13-](https://doi.org/10.5194/acp-13-89-2013)  
878 89-2013, 2013b.

879 Zhang, H., Li, J., Ying, Q., Guven, B. B., and Olaguer, E. P.: Source apportionment of  
880 formaldehyde during TexAQS 2006 using a source-oriented chemical transport model, *J.*  
881 *Geophys. Res.-Atmos.*, 118, 1525–1535, <https://doi.org/10.1002/jgrd.50197>, 2013.

882 Zhu, L., Jacob, D. J., Kim, P. S., Fisher, J. A., Yu, K., Travis, K. R., Mickley, L. J., Yantosca, R.  
883 M., Sulprizio, M. P., De Smedt, I., Abad, G. G., Chance, K., Li, C., Ferrare, R., Fried, A., Hair, J.  
884 W., Hanisco, T. F., Richter, D., Scarino, A. J., Walega, J., Weibring, P., and Wolfe, G. M.:  
885 Observing atmospheric formaldehyde (HCHO) from space: Validation and intercomparison of  
886 six retrievals from four satellites (OMI, GOME2A, GOME2B, OMPS) with SEAC<sup>4</sup>RS aircraft  
887 observations over the southeast US, *Atmos. Chem. Phys.*, 16, 13477–13490,  
888 <https://doi.org/10.5194/acp-16-13477-2016>, 2016.

889 Zhu, L., Jacob, D. J., Keutsch, F. N., Mickley, L. J., Scheffe, R., Strum, M., González Abad, G.,  
890 Chance, K., Yang, K., Rappenglück, B., Millet, D. B., Baasandorj, M., Jaeglé, L., and Shah, V.:  
891 Formaldehyde (HCHO) As a Hazardous Air Pollutant: Mapping Surface Air Concentrations  
892 from Satellite and Inferring Cancer Risks in the United States, *Environ. Sci. Technol.*, 51, 5650–  
893 5657, <https://doi.org/10.1021/acs.est.7b01356>, 2017.

894